HHS Public Access

Author manuscript

Adv Mater. Author manuscript; available in PMC 2024 August 01.

Published in final edited form as:

Adv Mater. 2023 August ; 35(31): e2302069. doi:10.1002/adma.202302069.

Renal Clearable Ultraminiature Chain-like Gold Nanoparticle Clusters for Multimodal Molecular Imaging of Choroidal Neovascularization

Phuc Nguyen Van[1], **Wei Qian**[2], **Josh Zhe**[1], **Jessica Henry**[1], **Mingyang Wang**[3], **Bing Liu**[2], **Wei Zhang**[3], **Xueding Wang**[3,*], **Yannis M. Paulus**[1,3,*]

[1]Department of Ophthalmology and Visual Sciences, University of Michigan, Ann Arbor, MI 48105, USA

[2]IMRA America, Inc., 1044 Woodridge Ave., Ann Arbor, MI 48105, USA

[3]Department of Biomedical Engineering, University of Michigan, Ann Arbor, MI 48105, USA

Abstract

Currently available gold nanoparticles (GNPs) typically accumulate in the liver and spleen, leading to concerns for their long-term biosafety. To address this long-standing problem, we developed ultraminiature chain-like gold nanoparticle clusters (GNCs). Via self-assembly of 7–8 nm GNP monomers, GNCs provide red-shifted optical absorption and scattering contrast in the near-infrared window. After disassembly, GNCs turn back to GNPs with a size smaller than the renal glomerular filtration size cutoff, allowing their excretion via urine. Our one-month longitudinal study in a rabbit eye model demonstrated that GNCs facilitate multimodal molecular imaging of choroidal neovascularization (CNV) *in vivo*, non-invasively, with excellent sensitivity and spatial resolution. GNCs targeting $\alpha_v\beta_3$ integrins enhanced photoacoustic and OCT signals from CNV by 25.3-fold and 150%, respectively. With excellent biosafety and biocompatibility demonstrated, **GNCs render a first-of-its-kind nanoplatform for biomedical imaging.**

Graphical Abstract

We developed first-of-its-kind multifunctional ultraminiature chain-like gold nanoparticle clusters (GNCs). Via self-assembly of 7–8 nm spherical GNP monomers, the GNC provides red-shifted optical absorption and scattering contrasts in the near-infrared (NIR) window which is highly desired by optical imaging modalities such as photoacoustic (PA) imaging and optical coherence tomography (OCT). After disassembly, the GNCs turn back into ultraminiature GNPs with a size smaller than the renal glomerular filtration size cutoff, allowing them to be excreted via urine

[*]Corresponding authors. Yannis M. Paulus, M.D., F.A.C.S., Department of Ophthalmology and Visual Sciences, Department of Biomedical Engineering, University of Michigan, 1000 Wall Street, Ann Arbor, MI 48105, USA, ypaulus@med.umich.edu, Xueding Wang, Ph.D., Department of Biomedical Engineering, Department of Radiology, University of Michigan, xdwang@umich.edu.

Author contributions: V.P.N. performed the experiments, and data analysis. W.Q. and B.L. were carried out GNPs fabrication, bioconjugation and their physiochemical characterization. W.Z. helped with fixing the photoacoustic and OCT scanner. M.H., J.Z and J.H. helped with in vitro PAM and OCT. X.W. and Y.M.P. supervised the project. V.P.N., W.Q., J.H., X.W., and Y.M.P composed the manuscript. All authors were participated in critical reviewing and revising of the manuscript.

Competing interests: The authors declare no competing interests.

instead of being trapped in the liver and spleen. Renal-clearable ultraminiature GNCs facilitate long-term multimodal molecular imaging of choroidal neovascularization *in vivo.*

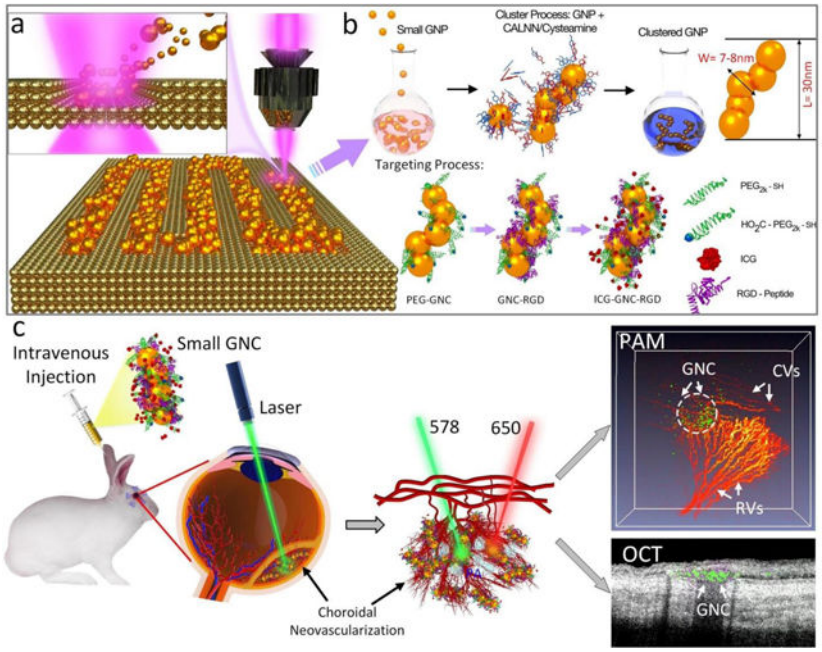

Keywords

Renal-clearable ultraminiature chain-like gold nanoparticles; photoacoustic microscopy; optical coherence tomography; retinal diseases; age-related macular degeneration; multimodality molecular ocular imaging; contrast agents

INTRODUCTION

Advanced non-invasive photoacoustic microscopy (PAM) and optical coherence tomography (OCT) imaging have been investigated and attracted significant attention as promising techniques to evaluate disease pathogenesis, such as cancer and angiogenesis, and treatments, such as stem cell therapy(1–8). The PAM and OCT signals are generated from the optical absorption and the optical scattering properties of the biological tissues, respectively, which can provide both anatomical and functional information. Most living organism tissues show low endogenous absorption and scattering of light in the red and near-infrared (R/NIR) spectrum (i.e., 600–1200 nm) which serves as an “optical window” for PAM and OCT-based molecular imaging powered by exogenous contrast agents.

Currently, there are several R/NIR PAM and OCT photosensitizers, including genetically encoded chromophores(1), small-molecular NIR dye (indocyanine green (ICG), IRDye800, CDnir7, ATTO740, SiNc), semiconductor and organic nanofluorophores in the second near-infrared (NIR-II) window(9, 10) as well as nanostructures made from carbon (e.g. carbon nanotubes, graphene-based nanomaterials and nanodiamonds), and gold (e.g., sphere, stars, tripods, plates, rods, and prisms)(11–14). Although some of the small molecular R/NIR dyes (e.g., ICG) are approved by the U.S. Food and Drug Administration (FDA) for clinical

utilization, these imaging materials have limited photostability and surface functionalization for active targeting. Gold nanoparticles (GNPs) show great potential as an emerging class of contrast agents in PAM and OCT imaging due to their excellent biocompatibility, low cytotoxicity, size-/shape-dependent superb optical absorption and scattering up to five orders of magnitude higher than those of traditional organic dyes, easy method of fabrication, and rich surface chemistry for functionalization. Despite significant progress in the last two decades on developing GNPs as contrast agents for molecular biomedical imaging, *in vivo* utility of conventional spherical GNPs in PAM imaging is restricted as a result of the overlapping of their localized surface plasmon resonance (LSPR) absorption peak (~520 nm) with that of hemoglobin.

As a first step towards overcoming such limitations, we recently developed chain-like gold nanoparticle cluster (GNC) via a method of self-assembly 20-nm GNPs fabricated by physical method using pulsed laser ablation (PLA)(5, 6, 15). The PLA technique was developed to assist with biomedical translation since it is a pure method lacking the toxic chemicals used in wet-chemical synthesis. PLA utilizes sterile deionized water and produces stable, nontoxic, and capping-agent free GNP monomers with high purity. This is different from chemical manners that comprise of toxic precursors, such as reducing substances and stabilizers. With a narrow gap (~1.0 nm) between adjacent GNPs in a chain, these GNC demonstrate a desired, red-shifted plasmonic absorption peak (longitudinal SPR) at the optical wavelength of 650 nm. In the experiments using multiple clinically relevant model of age-related macular degeneration (AMD) with the new development of blood vessels termed choroidal neovascularization (CNV) in large animals (rabbits), we have demonstrated that these GNC have excellent targeting efficiency, contrast enhancement, biocompatibility, and photostability.

When utilized as a novel contrast material for PAM and OCT multimodal molecular imaging, the angiogenesis-targeting GNC achieved a 17-fold enhancement in PA signal, facilitating highly sensitive detection and visualization of CNV in rabbit eyes *in vivo*(5). However, after intravenous administration, the majority of these GNC accumulate in the liver and spleen, leading to concerns about their long-term biosafety. This problem is common and shared by a variety of designs of GNPs with sizes larger than 10 nm. Mitchell *et al.* have reported that GNPs with a size smaller than 10 nm are rapidly eliminated by the kidneys(16). To address this problem, we have successfully developed a first-of-its-kind ultraminiature GNC composed of 7–8 nm spherical GNPs. Because the sizes of individual spherical GNPs forming the chains are smaller than the effective renal glomerular filtration size cutoff (6–10 nm), these ultraminiature GNC, while offering optical contrast enhancement in the red regime, can be renally excreted.

It is worth emphasizing that various types of renal clearable nanoparticles (NPs) and nanoclusters (NCs) have been developed since the pioneering work by Choi *et al.* on renal clearable quantum dots in 2007(17). Especially, in 2011, Chen *et al.* first reported the high efficiency renal clearance of glutathione-coated gold NCs with core sizes of 1–3 nm(18). Due to their efficient renal clearance, these gold NCs have become one of the most extensively studied inorganic renal clearable NPs/NCs over the last decade. In comparison to gold NCs, the novelty of the renal clearable ultraminiature chain-like gold NP clusters

(GNCs) demonstrated in our work lies in their unique shape, enhanced optical properties, improved performance, multifunctionality, and sustainability.

GNCs are elongated structures made up of multiple gold NPs linked together in a linear arrangement with a length in the range of tens of nanometers, whereas gold NCs, typically consisting of several to tens of gold atoms, are spherical with a size on the order of a few nanometers. The shape of gold NPs can affect their optical and electronic properties. Due to the plasmonic coupling between adjacent NPs, the elongated shape of GNCs gives them enhanced optical absorption and scattering properties, which is not present in gold NCs, although, their small size leads to unique properties like quantum confinement effects and size-dependent fluorescence. As described in our work, the enhanced optical properties of GNCs enable them to be used as contrast agents for creating highly sensitive multimodal photoacoustic microscopy (PAM) and optical coherence tomography (OCT) imaging. In contrast, gold NCs, exhibiting discrete absorption bands in the visible region, are not well-suited for these applications. Moreover, the peak wavelength of the enhanced optical absorption and scattering exhibited by GNCs is tunable and can be extended into the near-infrared (IR) region by manipulating their lengths(15). This distinctive feature makes GNCs a superior choice for biomedical imaging due to the deep penetration depth of near-IR photons.

Another advantage of GNCs is their easy and controllable surface functionalization property. In our previous publication, we showed that GNCs fabricated in this study allow versatile surface functionalization to achieve the conjugation of multiple types of ligands with predetermined amounts due to the capping-agent-free surface of the gold NP monomers used in the formation of the GNCs(19–21). This unique property enables to overcome the long-standing challenge of developing nanomaterial-based probes for in vivo multimodal molecular imaging that demand excellent colloidal stability, outstanding biocompatibility, and highly effective targeting capabilities, in which precise quantitative control over the surface modification of multiple types of functional ligands is necessary to accomplish these goals. Unlike GNCs, gold NCs are typically coated with a compact layer of organic ligands to prevent aggregation or oxidation. However, this coating inhibits the use of the rich gold chemistry for facile binding of functional biomolecules, making it difficult to achieve precise surface modification.

Finally, the GNCs are synthesized using a novel and environmentally friendly method called pulsed laser ablation (PLA). PLA has been chosen as the preferred method because it is a completely green synthesis that produces colloidal stable and capping-agent-free gold NP monomers directly in deionized (DI) water. Nevertheless, gold NCs are generally synthesized using wet-chemical methods. These methods involve chemical precursors, reducing agents, as well as stabilizing/capping ligands, all of which could have negative environmental impacts.

Besides the benefit of largely improved biosafety, these ultraminiature GNC also generate stronger PA signals than their absorption-matched counterparts due to the fact that PA signal amplitude is proportional to the surface-to-volume ratio of the NPs(12). To validate the ultraminiature GNC as a multimodal imaging contrast agent and to demonstrate their urinary

excretion, we performed *in vivo* longitudinal PA and OCT molecular retinal imaging in two clinically relevant rabbit models of CNV diseases: laser induced retinal vein occlusion (RVO) and subretinal injection of vascular endothelial growth factor (VEGF) and Matrigel. To achieve specific targeting to the angiogenesis in the choroid, the ultraminiature GNC, after fabrication, were conjugated with linear arginine-glycine-aspartate (RGD) peptides (i.e., GNC-RGD). They were then administered into the rabbits by intravenous injection route to examine their performance in molecular imaging of CNV, as well as their biosafety.

RESULTS

Fabrication and characterization of red-light absorbing ultraminiature GNC

In our development of the PLA method for the fabrication of GNPs, we observed that the size of the generated GNP monomers could be reduced by producing them in DI water containing a micromolar (μM) concentration of NaCl. Spherical GNP monomers with a mean diameter of 7–8 nm utilized in the formation of ultraminiature GNC for the present studies were fabricated by femtosecond PLA of gold target in 100 μM NaCl aqueous solution as shown in Figure 1a. Following the fabrication of these GNP monomers, an established method described in our previous publications(5) was used to self-assemble them into red-light absorbing GNC (Figure 1b). Briefly, this self-assembly was implemented by transforming the surface of 7–8 nm spherical GNP monomers with pentapeptides having an amino acid sequence Cys-Ala-Leu-Asn-Asn (CALNN) and small molecules, cysteamine. The colloidal solution of GNP monomers was sequentially mixed with CALNN peptides and cysteamine. The mixture was maintained at room temperature for approximately 24 h to 72 h until its color changed from pink-red to blue. The absorption spectrum of the mixture solution was determined to confirm the successful self-assembly of GNPs to ultraminiature GNC. To prevent the formation of a protein corona on the surface of the ultraminiature GNCs in vivo, we modified them with poly(ethylene glycol) (PEG), a well-known and effective method for avoiding protein adsorption in vivo because of the fact that PEG moieties on the NP surface create steric hindrance for protein adsorption(22, 23) and the high resistance of the obtained GNCs to protein binding was confirmed via in-vitro test using aqueous solution of bovine serum albumin (BSA) with mass concentration as high as 5 mg/mL(see Supplementary Figure S1a). For purposes of *in vivo* targeting of angiogenesis and fluorescence imaging, the ultraminiature GNC were then conjugated with Arg-Gly-Asp (RGD) peptides and near-infrared ICG dyes (Figure 1b). The morphologies of a single ultraminiature GNC (top) and a large GNC (bottom) composed of 20 nm diameter GNPs were visualized by transmission electron microscopy (TEM) (Figure 1c), where the chain structure is formed by 3–6 individual GNPs. The synthesized ultraminiature GNC had an optical absorption peak shifted from 520 nm to 610 nm (Figure 1d) when compared with that of the GNP monomers. As shown in the TEM images (Figure 1c), the sizes of the ultraminiature GNC are approximately 30.0 ± 2.1 nm (length) by 7.8 ± 1.1 nm (width). In addition, their hydrodynamic particle size distribution was determined via dynamic light scattering analysis which revealed an average size of 55.3 nm with polydispersity index of 0.3 (Figure 1e). Furthermore, zeta potential of the synthesized ultraminiature GNC was measured to be around −41 ± 2 mV, which allowed to achieve an excellent colloidal stability

demonstrated by no obvious change in the absorption spectra over time for up to two months (supplementary Figure S1b).

Finally, the loading efficiency of ICG and amount of RGD peptide on surface of ultraminiature GNCs were determined using a method involving DLS size measurement described in our previous papers(19, 21, 24). It was concluded that the loading efficiency of ICG is nearly 100% (or 25 ICG molecules per GNC) because the amount of ICG initially added is below that necessary for saturating surface of GNCs and there were about 200 RGD peptides on the surface of individual ultraminiature GNCs. Since the number of ICG molecules contained within individual GNCs is very small and did not change the peak absorption of GNC after conjugation (Supplementary Figure S1c), except for fluorescence imaging, the signal for the other two imaging modalities (PAM and OCT) reported in this study is generated directly from the GNCs.

As a reference for comparing the photoacoustic performance and the photostability of the GNC, we also fabricated GNC composed of 20-nm GNPs (named large GNC henceforth). For the synthesized large GNC, their average size was approximately 64 nm (length) by 20 nm (width), as shown in the TEM images (Figure 1c), and their red-shifted longitudinal SPR was controlled to be around 650 nm, for matching to that of the ultraminiature GNC as much as possible.

Targeting efficiency, *in vitro* photostability, and PA performance of the ultraminiature GNC

We first examined the targeting efficiency of the ultraminiature GNC. RGD peptides and ICG dyes were capped on the surface of the synthesized GNC (Figure 1b). The presence of RGD and ICG were confirmed by FT-IR analysis (Figure S1d). In our previous study, we have shown that RGD peptides have a great ability to target newly developed retinal vessels(5, 25, 26). ICG is approved by the FDA for use in ophthalmology and is thus a great fluorophore candidate for *in vivo* molecular imaging(27). The targeting specificity of the GNC was examined on human retinal pigment epithelial (ARPE-19) cells with differentiated properties, human umbilical Vein Endothelial Cells (HUVEC) and HeLa cells with and without RGD conjugation using laser scanning confocal microscope (Figure 1f and supplementary Figure S2). The results show that GNC (red color) accumulated in the cytoplasm (yellow color) of the cells, confirming the targeting specificity of RGD-conjugated GNC. The internalized ultraminiature GNC inside the cells could also be visualized using PA microscopy (PAM) imaging (Figure 1g–h), which illustrates that our custom-built multimodal PAM and OCT system (supplementary Figure S3) has a great capability to detect the accumulation of ultraminiature GNC inside single cells with excellent contrast and resolution (Figure 1h).

To evaluate the potential decay of PA signals caused by photo-damage of the ultraminiature GNC under nanosecond pulsed laser irradiation, as seen by changes in their UV-Vis absorption spectrum, colloidal solutions of both ultraminiature and large GNC were exposed to 75,000 laser pulses at various laser fluences (i.e., 0.005 to 0.04 mJ/cm^2). The relative PA signal amplitudes at each fluence were recorded and the absorption spectra of the ultraminiature GNC suspended solutions post pulsed laser irradiation were also measured (see Supplementary Note 3). At the highest laser fluences of 0.04 mJ/cm^2, PA signals

of both the large GNC and the ultraminiature GNC were stable and showed no obvious changes (Figure 1i). The fluctuation of the PA signal amplitude was primarily caused by the intensity variation of the laser system operated at 650 nm. To determine the laser threshold capable of disassembling GNC into GNP monomers, we increased the laser fluence to 8 and 10 mJ/cm^2. Working at 10 mJ/cm^2, we found that the PA signal amplitude reduced about 3.9-fold for the ultraminiature GNC and 6.7-fold for the large GNC after 6,000 pulses (Figure 1j). The decay of the PA signal amplitude could be due to the disassembly of the ultraminiature GNC since during the laser irradiation of solutions containing the ultraminiature GNC, the color of solutions gradually changed from blue to pink-blue for the ultraminiature GNC and to pink-red for the large GNC (Figure 1k). The disassembly of the GNC were further examined by the observed optical absorption spectra of the samples after laser illumination as shown in Figure 1 l–o. The results show that the peak absorption of the large GNC have shifted from 650 nm to 520 nm after being treated by 1200 pulses of 650-nm laser beam at both 8 and 10 mJ/cm^2 (Figure 1l and n). In contrast, the peak absorption of the ultraminiature GNC was only moderately changed after being irradiated by 1200 laser pulses. Even after being illuminated by 6000 laser pulses at 10 mJ/cm^2, the ultraminiature GNC still kept a relatively broad optical absorption spectrum (Figure 1m and o). This confirms that ultraminiature GNC have better photostability compared to the large GNC.

To compare PA and OCT signals generated by the ultraminiature and the large GNC, we acquired PAM and OCT images for samples, made from silicon tubes and glass tubes, containing either the ultraminiature or the large GNC at two different mass concentrations and for control sample filled with saline (Figure 2a–d). The PAM images show that the ultraminiature GNC provide higher contrast enhancement than the large GNC (Figure 2a), whereas OCT image contrast of the sample filled with the large GNC is higher than that of the ultraminiature GNC (Figure 2c). The PAM signal of the ultraminiature GNC exhibits 3.03-fold and 1.99-fold higher than that of the large GNC at mass concentration of 100 ug/mL (PA signal = 84.4±1.4 (a.u.) for the ultraminiature GNC and 27.9±2.6 (a.u.) for the large GNC) and 250 ug/mL (PA signal = 238.2±8.5 (a.u.) for the ultraminiature GNC and 119.7±6.4 (a.u.) for the large GNC), respectively (Figure 2b). Compared to the background, the ultraminiature GNC at 250 ug/mL enhanced the PA signal about 118.2-fold (PA signal = 0.2±0.1 (a.u.) for background). By quantification of the OCT signal extracted from the targeted areas on the OCT images, the OCT intensity of the ultraminiature GNC is 1.65-fold lower than that of the large GNC at 100 ug/mL (OCT signal = 79.5±9.4 (a.u.) for the ultraminiature GNC vs. OCT signal = 167.3±5.7 (a.u.) for the large GNC). However, there was not significant difference between these two samples at higher mass concentration of 250 ug/mL (OCT signal = 182.5±2.3 (a.u.) for the ultraminiature GNC vs. OCT signal = 207.4±8.5 (a.u.) for the large GNC) as shown in Figure 2d. The observed stronger PA signal of ultraminiature GNC than that of large GNC can be explained by that PA signal is proportional to the surface-to-volume ratio of the NPs, a mechanism reported by Gambhir and Emelianov[9], while large GNC scatter more light, leading to induced stronger OCT signal than that of ultraminiature GNC. We further examined the OCT signal of the ultraminiature GNC at different concentrations. We found that the OCT intensities were

linearly dependent on the concentration of both the ultraminiature and the large GNC. The minimal detectable concentration is 1 pg/mL (Figure 2e–f).

Biocompatibility, disassembly ability, and renal excretion Analysis,

We first evaluated the potential toxicity of the ultraminiature GNC *in vitro* and *in vivo*. Cytotoxicity analysis shows that the ultraminiature GNC induced mild decrease in cell viability on HUVEC, HeLa, and ARPE-19. The cell viability is more than 80% after treated with 500 μg/mL of the ultraminiature GNC for 48 h (Figure 3a and 3c, and Supplementary Figure S4a). To observe any potential of photothermal effect which could cause cell death after pulsed laser irradiation, MTT assay analysis of cells was performed after they were incubated with the ultraminiature GNC followed by laser irradiation at various fluences (i.e., 0.0025 to 0.08 mJ/cm^2). A quantitative cell viability assay demonstrated a mild decrease in the viable cell population, and the percentage of live cells was approximately 80% at 48 h post laser irradiation (Figure 3b and 3d, and Supplementary Figure S4b).

The cytotoxicity was further investigated using flow cytometry to determine the percentage of apoptotic cells caused by internalized ultraminiature GNC with and without laser illumination (Figure 3e). The results show that ultraminiature GNC induced mild apoptosis to the cells after treatment even after an incubation time of 48 hrs. Compared to the control, the population of viable cells is not significantly changed for the groups treated with ultraminiature GNC (live = 92.05% for control vs. 91.12% and 90.07% for GNC at 24 hrs and 48 hrs). The percentage of the apoptotic cell population is only about 1–2% higher than that of the control group (apoptosis = 1.58% for control vs. 3.64% and 4.01% for GNC at 24 h and 48 h). In addition, the results also illustrate that incubation with ultraminiature GNC followed by laser irradiation of 0.01 and 0.02 mJ/cm^2 only induced minimal toxicity to the cells. Biodistribution of GNC in organs show that some of them still accumulate in the spleen and kidney (Figure 3f) although the ultraminiature GNC can possibly escape from the RES system and be cleared from the body via the renal system as shown in Figure 3l. However, the amount of the ultraminiature GNC in liver and kidney were significantly lower than that of the large GNC. We then investigated on the disassembly of the ultraminiature GNC in liver tissues and found that small amounts of GNPs were observed on the TEM image of the tissue treated with ultraminiature GNC (Figure 3g). In contrast, a large amount of GNPs was accumulated in the cytoplasm of the group treated with large GNC and 60-nm GNPs (Figures 3h–i). This illustrates that the ultraminiature GNC can disassemble and thereby enhance clearance from the liver at 1-month post treatment. The efficient disassembly of ultraminiature GNC inside live cells were further confirmed by TEM Figure 3j–k). The results demonstrate that ultraminiature GNC were accumulated in the cytoplasm (Figure 3j) and broken into 7–8 nm GNP monomers at day 7 post treatment (Figure 3k).

The renal excretion ability of the ultraminiature GNC was evaluated and compared with the large GNC and GNP monomers in living rabbits. The ultraminiature and the large GNC and large GNP monomers were conjugated with RGD peptides and ICG dyes, and intravenously administrated into the rabbits at a volume of 400 μL (5 mg/mL). The collected urine solutions were imaged with a fluorescent imaging system for both pre- and post-injection at different time points (Figure 3l). No fluorescent signal was observed for the large GNC

and GNP monomer samples at any time after injection, whereas for the ultraminiature GNC, fluorescent signal reaches maximum at 2 h post injection before gradually reducing over time (Figure 3m). The amounts of GNC in the urine at different time points ranging from 2 h to 4 days were measured by inductively coupled plasma mass spectrometry (ICP-MS) technique and estimated to be 3.3×10^4 ppb at 2 h post injection. The renal excretion of the ultraminiature GNC were observed up to 7 days (Figure 3n). To further evaluate the distribution of GNC in urine as a result of renal clearance, we implemented an extra experiment by euthanized the animal at 6 hrs post I.V. injection of GNC at a volume of 400 μL (5 mg/mL). The organs and urine were harvested for ICP-MS and UV-vis spectrometer analysis. The ICP-MS data (Figure S5a) demonstrates that most GNC were detected in urine sample with higher rate than that of in other organs, illustrating that the administered GNCs were able to be cleared from the body via urine pathway. We also found that the accumulation of GNCs in kidneys is quite low. This can be explained by the short retention period of GNCs in kidneys as a result of their one-dimension linear structures. This is consistent with the results obtained by Ruggiero et al. who reported enhanced renal excretion of rod-shaped nanostructures due to flow-induced orientation, which caused a renal clearance of 65% of the injected dose within 20 min(28, 29). In addition, large molecules/particles were filtered faster than the small ones because the smaller ones are physically retained by the stationary phase for a longer period(30).

The absorption spectrum of urine was further characterized and plotted in Figure S5b. There is an absorption peak observed at 550 nm which is associated with the peak absorption of gold nanoparticles (GNPs) generated after the disassembly of GNCs. This result confirms the distribution of GNPs in urine which is consistent with ICP-MS data and fluorescent images (Figure 3l). To assess blood circulation half-life ($t_{1/2}$) of the ultraminiature and the large GNC, blood was drawn at 15 min, 2 h, 4 h, 1 day, 2 days, 3 days, and 7 days post injection, and the amount of GNC were determined using ICP-MS as shown in Figure 3o. The data shows that the large GNC have a circulation half-live of 0.5 h whereas the ultraminiature GNC have a significantly extended circulation half-life of approximately 4 hrs.

In vivo biosafety was carefully examined using different methods. The body weight of the treated animal was monitored at different time points for up to 1 month (Figure 4a). The data shows that all treated animal weights gradually increased, confirming nanoparticles induce minimal toxicity at the tested concentration. We further performed liver and kidney function tests (LFTs and KFTs) on mice and rabbits. We first tested the dose effect of ultraminiature GNC in mice by administrating them at different concentrations from 2.5 to 20.0 mg/kg and followed up to 30 days (N=3 per group). Both LFTs and KFTs show that blood urea nitrogen (BUN), alkaline phosphatase (ALP), and alanine amino transferase (ALT) at all tested levels were normal (Table S1), illustrating no severe damaged of liver and kidney function or systemic toxicity. In addition, LFTs and KFTs were also performed on rabbits post administration. There were no adverse changes in ALT, BUN, and ALP, indicating that ultraminiature GNC are biocompatible to the animal at low concentrations (Table S2). To determine the threshold of the GNC that cause a toxic effect on the kidney and liver, we administrated ultraminiature GNC and large GNC at a high concentrations of 2,200 and 8,800 mg/kg, respectively, and followed the animals for 7 days (N=3 per

group). We found that the body weight of the treated animal rapidly reduced and exhibited 35% loss post treatment (Figure 4b). In addition, the level of ALT, BUN, and ALP were higher than normal range (Table S3). This indicates that LFTs and KFTs of the animals could be affected by GNC at a high concentration. We further performed histological and TUNEL assay analyses on the treated tissues to examine whether administered GNC had a long-term toxicity. The cellular morphology fragmentation and tissue structure damage were not observed on the hematoxylin and eosin images achieved from the control and treated groups at low concentration (Figure 4c and h). In contrast, there was evidence of tissue structural changes observed in the liver, kidney, lung, spleen, and heart samples treated with a high concentration of large GNC (Figure 4d). Minimal tissue damage was found on the liver and spleen treated with a high concentration of ultraminiature GNC (Figure 4e). Minimal evidence of cells undergoing apoptosis was detected on TUNEL images obtained from sample treated with ultraminiature GNC at both high and low concentrations (Figure 4g and i). But significant numbers of apoptotic cells were found on the samples treated with high concentration of large GNC (Figure 4f). Figure 4j shows the positive control of spleen tissues.

Efficient molecular targeting of laser-induced choroidal neovascularization

To assess the feasibility of our ultraminiature GNC as multimodality PA and OCT molecular imaging contrast agents, we carried out multimodality PAM and OCT imaging by applying a clinically-relevant AMD disease model in rabbits, named choroidal neovascularization (CNV), as shown in Figure 5a. The CNV models were created by laser-induced retinal vein occlusion (RVO) with Rose Bengal (See Supplementary Note 6). We allowed the new developed CNV to stabilize at day 28 after RVO and day 7 after VEGF administration. Then, four groups of rabbit models were formed (RVO = 2 groups and VEGF injection = 2 groups) with each group containing three rabbits. Four groups with either RVO or VEGF injection received intravenous injection (I.V.) of non-targeted ultraminiature GNC or targeted ultraminiature GNC via RGD functionalization, respectively, through the marginal ear vein with the same injection amount of 400 μL at a mass concentration of 5 mg/mL. Longitudinal color fundus, fluorescence, PAM, and OCT imaging were obtained for both pre-injection and for up to 28 days post-injection. Color imaging and fluorescence angiography (FA) were used to monitor the development of CNV (Figure 5b–e). Leakage areas found in middle and late phase FA confirmed the evidence of the CNV lesion. PAM images were obtained along the scanning area (red dotted rectangle) shown in Figure 5b by exciting the rabbit retina at 578 nm and 650 nm with a fluence of 0.02 mJ/cm^2 and scanning the targeted region with an area of 4.5×4.5 mm^2. For rabbits injected with targeted GNC, strong PA signals were observed on the acquired PAM images at 650 nm after administration of the ultraminiature GNC (Fig. 5g, and Supplementary Figure S6), allowing easy observation and distinguishing of CNV from the adjacent healthy retinal and choroidal vessels as shown in Figure 5f. The location of CNV was longitudinally observed up to 21 days post injection with great contrast and then the PA signal amplitude decreased and was almost resolved by day 28 post administration. Selected co-registered three-dimensional PAM rendering obtained at 578 and 650 nm demonstrate better morphology of choroidal vessels (CVs), capillaries, retinal vessels (RVs), and CNV in 3D with high resolution (Figure 5h and Supplementary Videos 1 and 2). The margin and degree of CNV were significantly

distinguishable from the surrounding vessels. PAM depth view along XZ depicts the location of CNV lies between RVs and CVs (Figure 5i) and is co-registered well with 2D OCT image (Figure 5j). In contrast, for rabbits injected with non-targeted GNC, the PA signal was very low and almost undetected at the optical wavelength of 650 nm post nanoparticle's administration owing to lack of binding of GNC onto CNV (Figure 6).

The PA signals reached the maximum at 48 h post injection of targeted GNC and then gradually decreased over time (Figure 5l). When compared to pre injection, we observed a 25.3-fold increase in PA signal post injection of targeted ultraminiature GNC (PA_{signal} = 1.20 ± 0.01 (a.u.) for pre administration vs. 30.5 ± 1.2 (a.u.) for 48 h after administration; p=0.001). Remarkably, the PA signal obtained from using RGD-conjugated ultraminiature GNC was significantly higher than that obtained from using RGD-conjugated large GNC (Figure 5m). Compared to RGD-conjugated large GNC, RGD-conjugated ultraminiature GNC exhibited a 1.5-fold increase in PA signal (p=0.001). In addition, the ultraminiature GNC provided strong PA signal up to 21 days post injection, while large GNC only produced strong PA signal within 7 days post injection(5), gold nanorods (GNRs) targeted CNV up to 9 days(25), and gold nanostars (GNS) targeted CNV for up to 7 days(26). These results confirm better performance of the ultraminiature GNC in terms of enhancing PA signal and allowing prolonged longitudinal observation time compared to that of large GNC, GNR, and GNS. In addition, the ultraminiature GNC have a great photostability. There was no significant signal decay seen in the PAM images obtained at three different scans (Figure 7a). Spectroscopic PAM image (Figure 7b) exhibits that the CNV lesion were clearly detected and distinguished at wavelengths from 610 to 670 nm. The quantitative measurement of PAM signals at ROIs extracted from PAM images (Figure 7c) are consistent with the UV-vis absorption spectrum shown in Figure 1d.

Cross-sectional 2D OCT images were also obtained for both pre- and post-injection at different time points (day 1, 2, 3, 5, 7, 14, 21, and 28) as shown in Figure 8 and Supplementary Figure S7. CNV were clearly observed on the 3D volumetric OCT images obtained at 24 h post injection (Figure 8b) showing higher contrast than that of the one obtained pre-injection (Figure 8a). The CNV lesion was clearly found on the 3D image post injection. Cross-sectional 2D OCT image (Figure 8b1) and the further magnified one (Figure 8b2) display the depth location of CNV in the subretinal space with higher contrast in comparison with the pre-injection one (Figure 8a1). To better identify the margin and position of CNV, PAM images were co-registered with OCT images on the same imaging plane and displayed in Figure 8c and c1. The position of CNV were noticeably observed and discriminated from the surrounding vasculature. These results illustrate the great capability of multimodal PAM and OCT platform for precisely identifying newly developed microvasculature. Quantitative OCT signal intensity shows that the highest OCT signal peaked at 24–72 h post administration. Afterwards, this signal progressively reduced. Although the ultraminiature GNC generated strong OCT signal post injection, allowing easy visualization of CNV in the subretinal space, the OCT signal was only moderately increased by 51%. Compared to large GNC, OCT signal generated by ultraminiature GNC was about 20% lower, which could be attributed to their lower scattering efficiency. This result is consistent with the *in vitro* result (Figure 2a).

In vivo GNC targeting CNV after subretinal injection of Matrigel and VEGF

To evaluate the targeting efficiency of the synthesized ultraminiature GNC for visualization different ocular diseases, we further performed administration of the ultraminiature GNC in a rabbit model with subretinal administration of mixture Matrigel and VEGF-165 (Figure 9a). CNV generated from 3–7 days post Matrigel and VEGF injection was monitored by color fundus photography (Figure 5b) and indocyanine green angiography (ICGA) (Figure 9c–e). Color, early phase, and middle phase ICGA pictures clearly display architecture of retinal and choroidal vessels whereas the late phase ICGA image presents the CNV lesion due to leakage of ICG dye (Figure 9e). Figure 9f–g shows PAM images of the CNV obtained pre and post IV injection of the ultraminiature GNC at 24, 48, 72 hours, and days 5, 7, 14, 21, and 28, and at multiple wavelengths of 578 nm (Figure 9f) and 650 nm (Figure 9g). PAM images taken at additional times are presented in supplementary Figure S8. We found minimal PA signal in the 650-nm PAM image pre-injection. On the other hand, PA signal was significantly increased in the 650-nm PAM images obtained after treatment. Interestingly, the PA signal persisted up to 21 days post-injection (Figure 9g) and then nearly resolved by day 28. 3D PAM image generated at 578 nm and 650 nm were co-registered to facilitate visualization of the CNV lesion from the background signal from the surrounding CVs (Figure 9h and Supplementary Video 3).

The 3D OCT image (Figure 9j) acquired after administration of ultraminiature GNC also clearly exhibits the distribution of the GNC at the CNV lesion (white dotted circle), while minimal OCT signal was found in the 3D OCT image pre injection (Figure 9i). The co-registered PAM and OCT images confirmed the precise biodistribution of the GNC at the CNV. Figure 9l–m illustrates the 2D OCT image obtained along the scanning lines presented in Figure 9i–j. With the contrast enhancement by the GNC, CNV was better observed in the images captured after treatment in comparison to the pre-treatment images. The yellow dotted line shows the segment area of CNV. Thickness and areas of CNV were estimated to be 335.25 ±52.97 μm and 0.244 ±0.013 mm^2, respectively. The merged PAM and OCT images (Figure 9n) again confirm the capability of the multimodal imaging in the precise identification of CNV. Quantification of PA signal amplitude (Figure 9o) showed that PA signal amplitude significantly increased at 24 h and achieved peak absorption at 48 h post administration. Afterwards, the generated PA signal amplitude progressively declined over time. The graph shows that PA signals enhanced 18.4-fold at 48 h post administration when compared to pre-treatment (PA_{Signal}= 1.8 ± 0.8 (a.u.) for pre-treatment vs. 32.7 ± 2.2 (a.u.) for post-treatment, p=0.001).

DISCUSSION

The current study demonstrates successful development and utility of ultraminiature GNC as a contrast agent for multimodal PAM and OCT imaging. These results are very significant because they demonstrate a platform technology for biomedical molecular imaging. Benefiting from its unique design, the ultraminiature GNC have the optical absorption peak in the red and NIR window and are able to be renally excreted to improve their biosafety. As shown in this study, the ultraminiature GNC have largely reduced accumulation in the liver and spleen when compared to large GNC and large GNPs with

other designs. This study also shows that the formulation of the ultraminiature GNC has great photostability and biocompatibility when tested *in vivo* in a rabbit model. Compared to pre-injection, the ultraminiature GNC achieved a 25.3-fold enhance in PA contrast and a 150% enhance in OCT contrast in a rabbit CNV model. Another advantage of the synthesis the ultraminiature GNCs is that the GNC demonstrates great binding capability to $\alpha_v\beta_3$ integrins which is overexpressed in CNV in two different clinically-relevant rabbit models using physical method (RVO model) and chemical method (VEGF and Matrigel injection). Although the mechanism of CNV developement is different between these models, the RVO model triggers the release of various growth factors (e.g.,VEGF) via a the hypoxic effect, and VEGF delivered directly into the subretinal space via subretinal injection route, the ultraminiature GNCs demonstrated high targeting eficiency and could aid in visualization of both the position and the boundaries of CNV in 3D, permitting early diagnosis and therapy.

The study also conducted a comparison between large GNP monomers, large GNC, and ultraminiature GNC. The ultraminiature GNC had an absorption peak similar to that of large GNC but generated an increased PA signal due to their increased surface areas. The particles showed absorption primarily in the red (approximately 610 nm) optical window which might have ability to shift the optical absorption wavelength to NIR window (~650 nm) due to the accumulation of GNC at CNV, resulting in increased PA signals and help to distinguish CNV from the surrounding microvasculature, where there was a very low intrinsic PA signal from the background tissue such as hemoglobin (absorption coefficient: μa_{650} =1.98 cm^{-1}). The smaller size was of interest to this study because larger GNPs have been shown to accumulate in the liver and spleen, which raises long-term toxicity concerns(31). Current knowledge about the effect of NP size indicates that smaller size could penetrate the blood brain and blood-retinal barriers(32). However, this concern is alleviated by the biocompatibility of GNPs and the kidneys' ability to clear compounds less than 8 nm in size(33), which would indicate the compound could be efficiently excreted while maintaining an ideal residence time for image acquisition.

The toxicities related to the size of GNPs have been studied recently by several researchers(34, 35). Notably, Chen *et al.* discussed the size-dependent biological response of GNPs. They found that some larger sizes GNPs (8 to 37 nm) induced sickness in rats, while those in the range of 3 to 5 nm did not exhibit of sickness or lethality(35). Similarly, a study by Chou *et al.* reported size reduction in GNPs was associated with reduced long-term and short-term toxicity(36). This evidence demonstrates that ultraminiature GNC are ideal because they can be efficiently cleared over time, reducing long-term toxicity, while maintaining sufficient residence time to ensure they can be effective contrast agents. Their relatively higher molar mass in comparison to organic fluorochromes like ICG and Prussian blue allows them residence in CNV over time, providing strong PA signal amplitude at 2 h post administration, and subsequently can be cleared over the next 28 days through urine. However, there were some GNPs detected in spleen and liver at day 28 post injection (Figure 3f). This might be caused by the accumulation of some large GNC that could not clear from the urine. These GNPs might need additional time to disassemble into smaller GNP monomers in order to be cleared from the liver and spleen tissue through hepatic clearance, and lymphatic clearance(33). We also observed that the liver and renal functions of the animal were normal with no evidence of systemic toxicity when the animal received lose

or regular dose of the injection. On the other hand, severe toxicity was observed when the animal was injected at very high concentrations of large GNC (Figure 4b and Figure 4d–g). The potential toxicity of large GNC might be caused by the size-dependent toxicity, reactive oxygen species (ROS) production and immune response. Large GNCs (> 200 nm) may have a greater tendency to accumulate in certain tissues or organs such as the spleen and liver and may also be more difficult for the body to clear, leading to potential toxicity(20, 25, 26, 37, 38). The large size of the GNCs may also affect their interactions with biological molecules, such as proteins or cell membranes, which could lead to toxicity. The higher concentrations of GNCs the greater surface area to volume ratio of these particles causes their higher chemical reactivity and interaction of their surfaces with biological system. This interaction could potentially lead to increased production of ROS, which can cause oxidative stress, inflammation and consequent damages to the proteins, cell membrane and tissues(39–41). Large metal nanoparticles may be recognized as foreign and trigger an immune response, which could lead to acute inflammation to lung, liver and systemic damage(42, 43).

As demonstrated by this study, the ultraminiature GNC have the benefits of good *in vivo* stability in the short term, good photostability, and no cellular toxicity. The chains were gradually disassembled and cleared by 28 days post-administration. The study on imaging quality showed that the ultraminiature GNC allowed for effective PA imaging of CNV for 21 days post-injection. The PA signal enhancement in CNV over time was consistent, and the relatively larger change in PA signal enhancement due to the clearance of GNC was detectable only after 7 days post-injection. This duration is beneficial because it permits repeated imaging without the requirement of multiple injections. One shortcoming of the smaller size observed in the ultraminiature GNC is a slightly decreased OCT signal. However, this can be overcome by performing overlay images of PAM and OCT to better define CNV boundaries. The smaller GNC showed robust absorption efficiency in the red window, allowing their utility in imaging CNV using PAM at 650 nm. This wavelength is ideal since hemoglobin produces almost no PA signal at the optical wavelength of 650 nm, which enables differentiation of the biodistribution of photosensitizer materials from the native microvasculature with an injection of only 400 uL ultraminiature GNC at 5 mg/mL.

The investigation further supports the use of multimodal OCT and PAM for the detection of neovascularization in the sub-RPE. Many studies and clinical practices have investigated solely using OCT or OCTA. These methods are important for the visualization of healthy vasculature and conditions like RVO. However, these methods rely on backscattering light into target tissues, which limits their penetration depth(44). This study verified the hybrid biomedical imaging method of integrated PAM and OCT for imaging of CNV over time, benefiting from the non-invasive, 3-D imaging, and high spatial and temporal resolution nature of the PAM and OCT imaging modalities(45). Through this integration, OCT provides valuable structural and functional information(46), while PAM provides pertinent functional and molecular details(47–49).

While this system provides enhanced imaging of neovascularization in the subretinal location in the retina with excessive contrast and resolution, it still needs refinement prior to clinical translation. One of the current limitations is the lengthy image acquisition time, which is limited by the 1 KHz of pulse repetition rate of the optical parametric

oscillator (OPO) laser used for PAM. The current image acquisition time is roughly 65 s which could be significantly reduced by employing a high-speed laser system. Future investigation evaluating the clearance of GNC with various sizes, shapes, and formulations is also indicated. In addition, a more comprehensive understanding of GNC clearance can be performed in a future study to better understand the molecular pathology of GNCs.

In conclusion, this study validates the capability of biocompatible and photostable ultraminiature GNC as an excellent photosensitizer for PAM and OCT molecular imaging of a CNV rabbit model. The ultraminiature GNC exhibit a great optical property such as absorption and scattering efficiencies in the red-shifted spectral range around 610 nm. Also, these GNC are photostable even after thousands of pulses laser irradiation. Furthermore, they demonstrate excellent renal excretion which results in reduced long-term toxicity, while maintaining a relatively long residence in CNV. The *in vivo* data illustrates that PAM signal was enhanced up to 25.3-fold and OCT intensities were enhanced by 150% in comparison to pre-injection. Even at doses as low as 2 mg, these contrast enhancements permitted visualization of the position and margin of CNV with high sensitivity and high spatial resolution. The combination of the ultraminiature GNC and multimodal PAM and OCT yields high-contrast, 3-D volumetric imaging of CNV anatomy with sub-micrometer resolution.

MATERIALS AND METHODS

Targeting ultraminiature GNC labeled with ICG dye for retinal molecular imaging.

RGD functionalized ultraminiature GNC labeled with ICG dye (ICG@GNC-RGD) were fabricated as an imaging photosensitizer to improve high resolution multimodality fluorescence, PAM, and OCT imaging for evaluation of clinically-relevant disease models of CNV. Briefly, we first produced primary colloidal GNP spheres (7 – 8 nm) to be utilized for the synthesis of ultraminiature GNC via a laser-based method by ablating a massive fine gold sample (99.99%) in deionized water (18 MΩ cm) with a femtosecond pulsed laser beam, as described in our previous publication(19) and Supplementary Note 1, 2, and 3. In addition, it is worth mentioning that the GNPs fabricated by the pulsed laser ablation (PLA) technique are naturally negatively-charged without requiring capping ligands and stabilizing agents for retaining their colloidal stability and avoiding aggregation. This unique countenance allows versatile surface modifications(19), which is employed in this study to synthesize ultraminiature GNC.

The self-assembly processing of disperse GNPs into ultraminiature GNC was implemented by sequentially mixing the disperse GNPs solution with CALNN peptides and followed by cysteamine. In a typical process, 0.75 mL CALNN solution at concentration of 200 μM was added to a 50 mL sample of GNPs (7 – 8 nm) having an optical density (OD) of 1.0 at 512 nm. This mixture was maintained 2 h at room temperature to allow binding of CALNN ligands onto the surface of GNPs via gold-sulfur bonds. Afterwards, the mixture CALNN-GNPs were further conjugated with cysteamine molecules by adding 1.0 mL cysteamine at concentration of 200 μM. The mixed solution was kept undisturbed until observing a change of color from pink to blue.

The raw ultraminiature GNC were then labeled with NIR ICG dye and functionalized with RGD peptides for CNV targeting. Briefly, 50 mL colloidal solution of ultraminiature GNC with OD 1 at 610 nm was partially PEGylated by adding 0.1 mL PEG thiol-terminated (PEG-SH) with 2000 g/mol molar mass (PEG 2k-SH) with a concentration of 100 μM and kept undisturbed at room temperature for 2 h to enable sufficient conjugation of PEG 2k-SH onto the ultraminiature GNC. After the reaction, partially PEGylated ultraminiature GNC were labeled with ICG dye by the addition of 0.1 mL aqueous solution of ICG-PEG 2k-SH at a concentration of 100 μM. This mixture was left unperturbed for 2 h to allow ICG labeling (ICG-GNC). At the end, 1.0 mL RGD solution at a concentration of 200 μM was then added to the ICG-GNC. The solution was then left for 2 additional hours at room temperature to allow conjugation of RGD onto unoccupied sites of the ICG-GNC. The resultant solution was diluted with adding 50 mL of 4 mM borate buffer (pH 8.2) containing 8 mg/mL BSA and then was transferred into two 50 mL centrifugal tube for spinning down at 500 g for 2 h to a pellet. The final OD of the colloidal solution of PEGylated and RGD functionalized ultraminiature GNC labeled with ICG (ICG-GNC-RGD) was then adjusted to ~100 at 610 nm through resuspension of the pellet with borate buffer (4 mM, 8.2 pH) containing 4 mg/ml BSA after removal of the supernatant.

Photophysical properties of the RGD-conjugated ultraminiature GNC (GNC-RGD) and ICG-labeled GNC-RGD (ICG-GNC-RGD).

TEM image of colloidal GNPs and the ultraminiature GNC were obtained using JEOL 2010F operated at 200 kV. The maximum plasmonic absorption peak of GNPs and the ultraminiature GNC were determined from the optical wavelengths of 350 to 800 nm through use of a spectrophotometer (UV-3600, Shimadzu Corp., Japan). Surface zeta potential values and hydrodynamic nanoparticle size distribution were determined by a Zetasizer Nano ZS90 equipment (Malvern Instruments, Malvern, Worcestershire, UK). The IR spectra of GNP monomer, CALNN peptide, GNC, thiolated PEG 2000, and PEGylated GNC were evaluated by a FTIR spectrometer (PerkinElmer Inc., Waltham, MA).

The colloidal stability of the ultraminiature GNC was evaluated by measured the plasmonic absorption spectrum of the ultraminiature GNC sample incubated in serum and followed up for 1 month. Zeta potential values and particle size of the sample were also acquired. The potential redshift of NPs was also characterized in the biological environment (see Supplementary Note 1 and 3). Photostability of the synthesized NPs was determined by measured the plasmonic absorption spectrum of the samples after being exposed to nanosecond pulsed laser (650 nm and 75,000 pulses) at different fluences: 0.005, 0.01, 0.02, and 0.04 mJ/cm^2 and higher fluence of 8 and 10 mJ/cm^2 (see Supplementary Note 5).

In vivo renal clearance of GNC-RGD and half-life circulation.

To examine the renal clearance of the synthesized ultraminiature GNC-RGD in living rabbits, we performed analysis including fluorescence imaging and inductively coupled plasma mass spectrometer (ICP-MS) analysis. Three different GNP samples (disperse GNPs with a core diameter of 60 nm, GNC composed of 20 nm diameter GNP spheres, and ultraminiature GNC composed of 7–8 nm diameter GNP spheres) with the same concentration of 5 mg/mL were intravenously administered to the rabbits at a dose of 400

μL. Urine solutions were obtained from 2 h to day 7 post-injection. 5 mL of urine was added to an assay well on a 24-well tissue culture plate. Fluorescence images were captured at NIR wavelength of 800 nm with the exposure time of 1 ms using Azure 600 bioimaging system (Dublin, CA, USA). The fluorescent signal intensity was then measured using region of interest (ROI) analysis. The kinetics of GNC in urine was examined. The urine samples were then diluted in aqua regia solution (mixed nitric acid and hydrochloric acid with a ratio of 1:3) to determine the amount of GNPs in those samples using wet dissolve protocol as described in previous studies(5, 6, 25) (see Supplementary Note 4. The dissolved samples were mixed with 4 mL of D.I. water for the measurement using inductively coupled plasma mass spectrometer (ICP-MS) (Nexion 2000S, Perkin-Elmer, MA, USA).

The circulation time of GNPs in blood was also characterized using wet ICP-MS method. Briefly, 400 μL of blood samples were collected from the injected animal described above at different time points: 15 min, 45 min, 1, 2, 4, 8, 16, 24, 48, 72 h, day 4, 5, and 7. The collected blood samples were processed the same as the protocol applied for urine samples and the amount of GNPs in blood were determined by ICP-MS method.

In vivo biodistribution of the ultraminiature GNC-RGD and cytotoxicity analysis.

In vivo toxicity was tested on three groups of rabbits (N=3). These animals were intravenously injected with 400 μL of ultraminiature GNC, large GNC, and the PEGylated 20 nm diameter GNPs at the same concentration of 5 mg/mL via the marginal ear vein. The body weight of all animals including the control group were acquired daily for up to 1 month. After 1 month, 400 μL of blood sample was taken from all the animals. The samples were then centrifuged at 3,000 rpm for 4 min to isolate serum from red blood cells. The collected serum was used for mini chemistry panel analysis to validate the kidney and liver functions of the treated animal. Afterwards, all the rabbits were sacrificed, and the organs (liver, kidney, lung, heart, and spleen) and the eyeballs were isolated. These organ samples were sectioned into 2 g and kept in –20 ^{o}C to determine the amount of GNPs by ICP-MS (see Supplementary Notes 4). The remained sampled were fixed in 10% formaldehyde solution. The eye tissue was processed for histological, immunohistochemistry, and TUNEL assay analyses (see Supplementary Notes 4).

The potential toxicity of the GNC was further evaluated on mice. Five groups of mice (n=3 per group) were received tail vein injection of ultraminiature GNC and large GNC at different concentrations (0 (control), 5, 10, 20, 40, 2200, and 8800 mg/kg). The body weight of the treated mice was measured daily up to 7 days. Then, mice were sacrificed. Blood and organs were harvested for LFTs, KFTs and histological analysis (see Supplementary Notes 4).

Multimodal PAM and OCT retinal molecular imaging system.

A specialized, custom-modified, noninvasive multimodality PAM and OCT imaging platform is exhibited in the Supplementary Note 7, and Supplementary Figure S3a(47, 50). To generate the PA signal, nanosecond laser pulses (3–5 ns and pulse repetition rate of 1 kHz) from a Nd:YAG laser (NT-242, Ekspla, Lithuania) were used to excite the tissues. The optical wavelength of the excitation light from the OPO can be turned from 405 nm to 2600

nm to match the maximum absorption peak of the sample to achieve the optimal PA signal. The excitation light was filtered and controlled to establish a circular beam around 2 mm before illuminating the sample. For *in vivo* experiments, a laser fluence of 0.04 mJ/cm^2 was selected to excite the sample. Spectroscopy PAM was implemented by tuning the optical wavelength from 500 nm to 700 nm under the same excitation laser fluences. The generated PA signal was detected by an ultrasonic transducer with a center frequency of 27 MHz (Optosonic Inc., Arcadia, CA, USA)(51). The PAM system has lateral resolution of 4.1 μm and axial resolution of 37.0 μm. The preamplifier was used to augment the generated PA signal (AU-1647, gain 57 dB, L3 Narda-MITEQ, NY). The PA signal were then digitized by a DAQ card (PX1500–4, Signatec Inc., Newport Beach, CA). Amira 6.0 software was used to render 3D images and videos (Amira, FEI, Fisher Sci, USA).

Customized high resolution OCT imaging was established from a Ganymede-II-HR OCT device (Thorlabs, Newton, NJ) as reported in our previous studies(47, 50). The OCT system was combined with PAM system to achieve multimodality imaging platform. To do so, the OCT light source was coaxially integrated with the excitation light of the PAM system. OCT system used two superluminescent diodes (SLDs) with central frequencies of 846 nm and 932nm to illuminate the tissues. The OCT device has lateral resolution of 3.8 μm and axial resolution of 4.0 μm. The scanning area was 5.5 (length) × 5.5 (width) × 1.8 mm (depth) with a resolution of 512 × 512 × 1024 pixels.

In vivo GNC-RGD targeting of choroidal neovascularization.

All the animal experiments were implemented in accordance with experimental the guidelines of the Association for Research in Vision and Ophthalmology (ARVO) Statement and the approved protocols by the Institutional Animal Care and Use Committee (IACUC) at the University of Michigan (PRO000010388). Healthy New Zealand White rabbits both genders at age of 3–4 months old and weighting of 2.4–2.8 kg were utilized in this report. Choroidal neovascularization (CNV) in the rabbit model was created by two different methods: subretinal injection of Matrigel and human vascular endothelial growth factor (VEGF-165, Shenandoah Biotechnology, Warwick, USA) and laser-induced retinal vein occlusion with Rose Bengal (see Supplementary Note 7). In RVO-induced choroidal neovascularization, the blockage of the retinal vein causes a hypoxic environment in the retina, which triggers the release of various growth factors, including VEGF, that promote the growth of new blood vessels. In contrast, subretinal injection of Matrigel and VEGF directly introduces high levels of the growth factor into the eye, which can promote angiogenesis and the growth of new blood vessels. The CNV model was created about 1 month after laser photocoagulation or day 3–7 after administration of Matrigel and VEGF-165(5, 25, 27, 52, 53). Before imaging, rabbits were anesthetized using ketamine (40 mg/kg, 100 mg/mL) and xylazine (5 mg/kg, 100 mg/mL). 400 μL of NPs (ultraminiature GNC-RGD and PEGlated ultraminiature GNC) at concentration of 5 mg/mL were intravenously administrated into the animal models. PAM and OCT images were achieved before and after injection at various time points (2, 4, 24, 48 hours, and day 5, 7, 14, 21, and 28).

Transmission electron microscopy analysis.

Transmission electron microscopy (TEM) analysis was implemented to assess disassembly of GNC as reported in our previous study(6). Briefly, rabbits' livers were harvested and sectioned into $0.5\times0.5\times0.5$ mm^3. The samples were fixed in 2.5% glutaraldehyde solution in a 0.1 M Sorensen's phosphate buffer (pH = 7.4) for 24 h. Afterward, the samples were washed three times with Soren's buffer (0.1 M). The samples were dehydrated and polymerized before sectioning. The sample was sectioned with a thickness of about 70 nm using a microtome (Sorvall MT-2B, NY, USA). The specimens were placed into 200 mesh fine bar hex grids, stained with uranyl acetate and lead citrate. High resolution TEM images were captured using a transmission electron microscope (JOL-JEM 1400 Plus, Japan Electron Optic, Tokyo, Japan).

Statistical methods.

All the experiment conditions were replicated three times. The PAM and OCT signals were measured at each condition. ANOVA statistic was implemented to examine any significant difference between treatment groups. The final data was denoted as the average ± standard deviation (SD). *P*-values of < 0.05 exhibited as statistically significant. Noted that $*p<0.05$, $**p<0.01$, and $***p<0.001$

Supplementary Material

Refer to Web version on PubMed Central for supplementary material.

Acknowledgments

This work was funded by grants from the National Eye Institute (YMP:1K08EY027458, 1R01EY033000, 1R41EY031219), Fight for Sight-International Retinal Research Foundation (YMP: FFSGIA16002), Alcon Research Institute Young Investigator Grant (YMP), unrestricted departmental support from Research to Prevent Blindness, generous support of the Helmut F. Stern Career Development Professorship in Ophthalmology and Visual Sciences (YMP), and the University of Michigan Department of Ophthalmology and Visual Sciences.

We would like to acknowledge Dr. David A. Antonetti for providing the ARPE-19 cells, Dr. Abigail Fahim for providing the Human umbilical Vein Endothelial Cells (HUVEC), and Dr. Phil Kish and Dr. Prasov for support with the tissue culture. We thank Dr. Steve Lenz for assisting on confocal microscope analysis. We thank Drs. Yuqing Chen, Dongshan Yang and the University of Michigan CAMTraST for the substantial donation of rabbits.

Funding:

This work was funded by grants from the National Eye Institute (YMP:1K08EY027458, 1R01EY033000, 1R41EY031219), Fight for Sight-International Retinal Research Foundation (YMP: FFSGIA16002), Alcon Research Institute Young Investigator Grant (YMP), unrestricted departmental support from Research to Prevent Blindness, generous support of the Helmut F. Stern Career Development Professorship in Ophthalmology and Visual Sciences (YMP), and the University of Michigan Department of Ophthalmology and Visual Sciences. This research utilized the Core Center for Vision Research funded by the National Eye Institute (P30 EY007003).

Data and materials availability:

The data that support the plots and other findings of this study are available from the corresponding authors upon reasonable request.

References and Notes

[1]. Jathoul AP, Laufer J, Ogunlade O, Treeby B, Cox B, Zhang E, Johnson P, Pizzey AR, Philip B, Marafioti T, Lythgoe MF, Pedley RB, Pule MA, Beard P, Deep in vivo photoacoustic imaging of mammalian tissues using a tyrosinase-based genetic reporter. Nature Photonics 9, 239–246 (2015).

[2]. Shi J, Wong TTW, He Y, Li L, Zhang R, Yung CS, Hwang J, Maslov K, Wang LV, High-resolution, high-contrast mid-infrared imaging of fresh biological samples with ultraviolet-localized photoacoustic microscopy. Nature Photonics 13, 609–615 (2019). [PubMed: 31440304]

[3]. Wang LV, Multiscale photoacoustic microscopy and computed tomography. Nature Photonics 3, 503–509 (2009). [PubMed: 20161535]

[4]. Zhang W, Li Y, Nguyen VP, Huang Z, Liu Z, Wang X, Paulus YM, High-resolution, in vivo multimodal photoacoustic microscopy, optical coherence tomography, and fluorescence microscopy imaging of rabbit retinal neovascularization. Light: Science & Applications 7, 1–12 (2018).

[5]. Nguyen VP, Qian W, Li Y, Liu B, Aaberg M, Henry J, Zhang W, Wang X, Paulus YM, Chain-like gold nanoparticle clusters for multimodal photoacoustic microscopy and optical coherence tomography enhanced molecular imaging. Nature Communications 12, 1–14 (2021).

[6]. Nguyen VP, Fan W, Zhu T, Qian W, Li Y, Liu B, Zhang W, Henry J, Yuan S, Wang X, Long-Term, Noninvasive In Vivo Tracking of Progenitor Cells Using Multimodality Photoacoustic, Optical Coherence Tomography, and Fluorescence Imaging. ACS nano 15, 13289–13306 (2021). [PubMed: 34378374]

[7]. Huang D, Swanson EA, Lin CP, Schuman JS, Stinson WG, Chang W, Hee MR, Flotte T, Gregory K, Puliafito CA, Optical coherence tomography. Science 254, 1178–1181 (1991). [PubMed: 1957169]

[8]. Sauvage F, Nguyen VP, Li Y, Harizaj A, Sebag J, Roels D, Van Havere V, Peynshaert K, Xiong R, Fraire JC, Laser-induced nanobubbles safely ablate vitreous opacities in vivo. Nature nanotechnology 17, 552–559 (2022).

[9]. Wan H, Yue J, Zhu S, Uno T, Zhang X, Yang Q, Yu K, Hong G, Wang J, Li L, A bright organic NIR-II nanofluorophore for three-dimensional imaging into biological tissues. Nature communications 9, 1171 (2018).

[10]. Liu P, Shi T, Li H, Chen H, Huang Y, Ma H, Zhu T, Zhao R, Li Y, Xin Q, Airy beam assisted NIR-II light-sheet microscopy. Nano Today 47, 101628 (2022).

[11]. Weber J, Beard PC, Bohndiek SE, Contrast agents for molecular photoacoustic imaging. Nature Methods 13, 639–650 (2016). [PubMed: 27467727]

[12]. Chen Y-S, Zhao Y, Yoon SJ, Gambhir SS, Emelianov S, Miniature gold nanorods for photoacoustic molecular imaging in the second near-infrared optical window. Nature nanotechnology 14, 465–472 (2019).

[13]. De La Zerda A, Zavaleta C, Keren S, Vaithilingam S, Bodapati S, Liu Z, Levi J, Smith BR, Ma T-J, Oralkan O, Cheng Z, Chen X, Dai H, Khuri-Yakub BT, Gambhir SS, Carbon nanotubes as photoacoustic molecular imaging agents in living mice. Nature Nanotechnology 3, 557–562 (2008).

[14]. Li Z, Wang S, Zhao J, Luo Y, Liang H, Zhao S, Zhang L, Gold Nanocluster Encapsulated Nanorod for Tumor Microenvironment Simultaneously Activated NIR-II Photoacoustic/ Photothermal Imaging and Cancer Therapy. Advanced Therapeutics, 2200350 (2023).

[15]. McLean A, Kanetidis M, Gogineni T, Ukani R, McLean R, Cooke A, Avinor I, Liu B, Argyrakis P, Qian W, Au Nanobead Chains with Tunable Plasmon Resonance and Intense Optical Scattering: Scalable Green Synthesis, Monte Carlo Assembly Kinetics, Discrete Dipole Approximation Modeling, and Nano-Biophotonic Application. Chem. Mater. 33, 2913–2928 (2021).

[16]. Mitchell M, Billingsley M, Haley R, Marissa E, Nicholas A, Langer Robert. Engineering precision nanoparticles for drug delivery. Nat Rev Drug Discov 20, 101–124 (2021). [PubMed: 33277608]

[17]. Soo Choi H, Liu W, Misra P, Tanaka E, Zimmer JP, Itty Ipe B, Bawendi MG, Frangioni JV, Renal clearance of quantum dots. Nat. Biotechnol. 25, 1165–1170 (2007). [PubMed: 17891134]

[18]. Zhou C, Long M, Qin Y, Sun X, Zheng J, Luminescent gold nanoparticles with efficient renal clearance. Angewandte Chemie International Edition 50, 3168–3172 (2011). [PubMed: 21374769]

[19]. Qian W, Murakami M, Ichikawa Y, Che Y, Highly efficient and controllable PEGylation of gold nanoparticles prepared by femtosecond laser ablation in water. The Journal of Physical Chemistry C 115, 23293–23298 (2011).

[20]. Nguyen VP, Qian W, Li Y, Liu B, Aaberg M, Henry J, Zhang W, Wang X, Paulus YM, Chain-like gold nanoparticle clusters for multimodal photoacoustic microscopy and optical coherence tomography enhanced molecular imaging. Nature Communications 12, 34 (2021).

[21]. Tian C, Qian W, Shao X, Xie Z, Cheng X, Liu S, Cheng Q, Liu B, Wang X, Plasmonic nanoparticles with quantitatively controlled bioconjugation for photoacoustic imaging of live cancer cells. Advanced Science 3, 1600237 (2016).

[22]. Pelaz B, del Pino P, Maffre P, Hartmann R, Gallego M, Rivera-Fernandez S, de la Fuente JM, Nienhaus GU, Parak WJ, Surface functionalization of nanoparticles with polyethylene glycol: effects on protein adsorption and cellular uptake. ACS nano 9, 6996–7008 (2015). [PubMed: 26079146]

[23]. Liu J, Yu M, Ning X, Zhou C, Yang S, Zheng J, PEGylation and zwitterionization: pros and cons in the renal clearance and tumor targeting of near-IR-emitting gold nanoparticles. Angewandte Chemie 125, 12804–12808 (2013).

[24]. Chen H, Paholak H, Ito M, Sansanaphongpricha K, Qian W, Che Y, Sun D, 'Living'PEGylation on gold nanoparticles to optimize cancer cell uptake by controlling targeting ligand and charge densities. Nanotechnology 24, 355101 (2013).

[25]. Nguyen V-P, Li Y, Henry J, Zhang W, Wang X, Paulus YM, Gold Nanorod Enhanced Photoacoustic Microscopy and Optical Coherence Tomography of Choroidal Neovascularization. ACS Applied Materials & Interfaces 13, 40214–40228 (2021). [PubMed: 34403578]

[26]. Nguyen V-P, Li Y, Henry J, Zhang W, Aaberg M, Jones S, Qian T, Wang X, Paulus YM, Plasmonic gold nanostar-enhanced multimodal photoacoustic microscopy and optical coherence tomography molecular imaging to evaluate choroidal neovascularization. ACS sensors 5, 3070–3081 (2020). [PubMed: 32921042]

[27]. Nguyen VP, Folz J, Li Y, Henry J, Zhang W, Qian T, Wang X, Paulus YM, Indocyanine green-enhanced multimodal photoacoustic microscopy and optical coherence tomography molecular imaging of choroidal neovascularization. Journal of Biophotonics 14, e202000458 (2021).

[28]. Ruggiero A, Villa CH, Bander E, Rey DA, Bergkvist M, Batt CA, Manova-Todorova K, Deen WM, Scheinberg DA, McDevitt MR, Paradoxical glomerular filtration of carbon nanotubes. Proceedings of the National Academy of Sciences 107, 12369–12374 (2010).

[29]. Liu J, Yu M, Zhou C, Zheng J, Renal clearable inorganic nanoparticles: a new frontier of bionanotechnology. Materials Today 16, 477–486 (2013).

[30]. Du B, Jiang X, Das A, Zhou Q, Yu M, Jin R, Zheng J, Glomerular barrier behaves as an atomically precise bandpass filter in a sub-nanometre regime. Nature nanotechnology 12, 1096–1102 (2017).

[31]. Khlebtsov N, Dykman L, Biodistribution and toxicity of engineered gold nanoparticles: a review of in vitro and in vivo studies. Chem. Soc. Rev. 40, 1647–1671 (2011). [PubMed: 21082078]

[32]. De Jong WH, Hagens WI, Krystek P, Burger MC, Sips AJ, Geertsma RE, Particle size-dependent organ distribution of gold nanoparticles after intravenous administration. Biomaterials 29, 1912–1919 (2008). [PubMed: 18242692]

[33]. Longmire M, Choyke PL, Kobayashi H, Clearance properties of nano-sized particles and molecules as imaging agents: considerations and caveats. (2008).

[34]. Chen Y-S, Hung Y-C, Liau I, Huang GS, Assessment of the in vivo toxicity of gold nanoparticles. Nanoscale research letters 4, 858–864 (2009). [PubMed: 20596373]

[35]. Lasagna-Reeves C, Gonzalez-Romero D, Barria M, Olmedo I, Clos A, Ramanujam VS, Urayama A, Vergara L, Kogan MJ, Soto C, Bioaccumulation and toxicity of gold nanoparticles after

repeated administration in mice. Biochem. Biophys. Res. Commun. 393, 649–655 (2010). [PubMed: 20153731]

[36]. Chou LY, Zagorovsky K, Chan WC, DNA assembly of nanoparticle superstructures for controlled biological delivery and elimination. Nature nanotechnology 9, 148–155 (2014).

[37]. Chithrani BD, Ghazani AA, Chan WC, Determining the size and shape dependence of gold nanoparticle uptake into mammalian cells. Nano letters 6, 662–668 (2006). [PubMed: 16608261]

[38]. Jo D, Kim J, Lee T, Kim J, Nanomed.: Nanotechnol. Biol., Med 11, 1603 (2015).

[39]. Ahamed M, Karns M, Goodson M, Rowe J, Hussain SM, Schlager JJ, Hong Y, DNA damage response to different surface chemistry of silver nanoparticles in mammalian cells. Toxicol. Appl. Pharmacol. 233, 404–410 (2008). [PubMed: 18930072]

[40]. Wang F, Yu L, Monopoli MP, Sandin P, Mahon E, Salvati A, Dawson KA, The biomolecular corona is retained during nanoparticle uptake and protects the cells from the damage induced by cationic nanoparticles until degraded in the lysosomes. Nanomedicine: Nanotechnology, Biology and Medicine 9, 1159–1168 (2013). [PubMed: 23660460]

[41]. Sharma V, Shukla RK, Saxena N, Parmar D, Das M, Dhawan A, DNA damaging potential of zinc oxide nanoparticles in human epidermal cells. Toxicol. Lett. 185, 211–218 (2009). [PubMed: 19382294]

[42]. Devanabanda M, Latheef SA, Madduri R, Immunotoxic effects of gold and silver nanoparticles: Inhibition of mitogen-induced proliferative responses and viability of human and murine lymphocytes in vitro. J. Immunotoxicol. 13, 897–902 (2016). [PubMed: 27754724]

[43]. Hannon G, Lysaght J, Liptrott NJ, Prina-Mello A, Immunotoxicity considerations for next generation cancer nanomedicines. Advanced Science 6, 1900133 (2019).

[44]. Soetikno BT, Shu X, Liu Q, Liu W, Chen S, Beckmann L, Fawzi AA, Zhang HF, Optical coherence tomography angiography of retinal vascular occlusions produced by imaging-guided laser photocoagulation. Biomedical optics express 8, 3571–3582 (2017). [PubMed: 28856036]

[45]. Xu M, Wang LV, Photoacoustic imaging in biomedicine. Rev. Sci. Instrum. 77, 041101 (2006).

[46]. P Mattison S, Kim W, Park J, E Applegate B, Molecular imaging in optical coherence tomography. Current Molecular Imaging (Discontinued) 3, 88–105 (2014).

[47]. Tian C, Zhang W, Mordovanakis A, Wang X, Paulus YM, Noninvasive chorioretinal imaging in living rabbits using integrated photoacoustic microscopy and optical coherence tomography. Optics express 25, 15947–15955 (2017). [PubMed: 28789105]

[48]. Nguyen VP, Li Y, Zhang W, Wang X, Paulus YM, High-resolution multimodal photoacoustic microscopy and optical coherence tomography image-guided laser induced branch retinal vein occlusion in living rabbits. Sci. Rep. 9, 1–14 (2019). [PubMed: 30626917]

[49]. Nguyen VP, Li Y, Qian W, Liu B, Tian C, Zhang W, Huang Z, Ponduri A, Tarnowski M, Wang X, Contrast agent enhanced multimodal photoacoustic microscopy and optical coherence tomography for imaging of rabbit choroidal and retinal vessels in vivo. Sci. Rep. 9, 1–17 (2019). [PubMed: 30626917]

[50]. Tian C, Zhang W, Nguyen VP, Wang X, Paulus YM, Novel Photoacoustic Microscopy and Optical Coherence Tomography Dual-modality Chorioretinal Imaging in Living Rabbit Eyes. J Vis Exp, (2018).

[51]. Ma T, Zhang X, Chiu CT, Chen R, Shung KK, Zhou Q, Jiao S, Systematic study of high-frequency ultrasonic transducer design for laser-scanning photoacoustic ophthalmoscopy. Journal of biomedical optics 19, 016015 (2014).

[52]. Nguyen VP, Li Y, Zhang W, Wang X, Paulus YM, Multi-wavelength, en-face photoacoustic microscopy and optical coherence tomography imaging for early and selective detection of laser induced retinal vein occlusion. Biomedical Optics Express 9, 5915–5938 (2018). [PubMed: 31065403]

[53]. Li Y, Zhang W, Nguyen VP, Rosen R, Wang X, Xia X, Paulus YM, Real-time OCT guidance and multimodal imaging monitoring of subretinal injection induced choroidal neovascularization in rabbit eyes. Exp. Eye Res. 186, 107714 (2019).

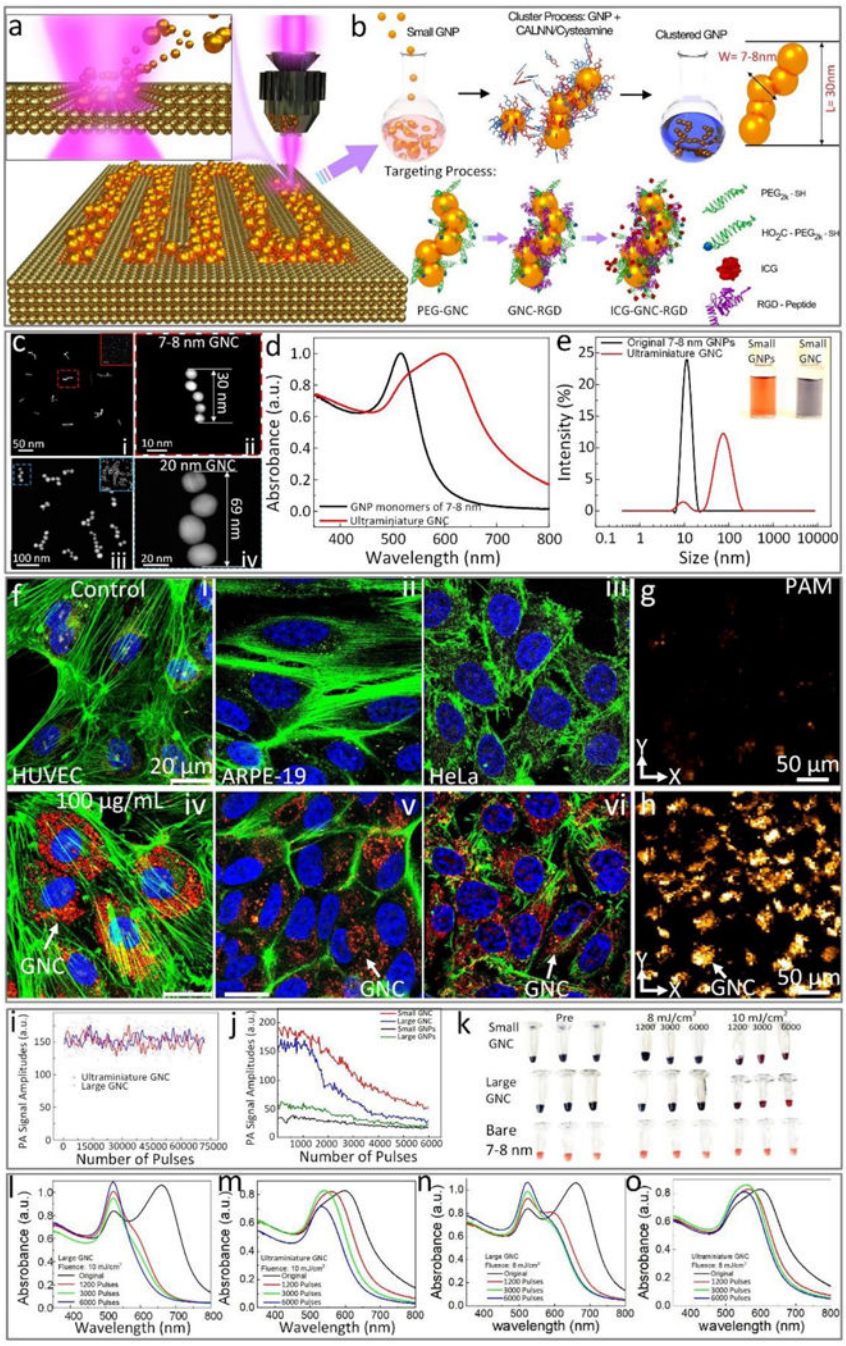

Fig. 1. Schematic and physiochemical characterization of the ultraminiature renal clearable GNC encapsulated with RGD ligands (GNC-RGD).

(a) Schematic of physical fabrication of 7–8 nm diameter GNP spheres using pulsed laser ablation (PLA) method. Colloidal 7–8 nm diameter GNP spheres fabricated by PLA method were self-assembled using cysteamine and pentapeptide Cys-Ala-Leu-Asn-Asn (CALNN) to form a chain-like structure. Then, GNC were encapsulated with RGD ligands (GNC-RGD) and ICG dyes to form ICG-GNC-RGD (b). (c) Transmission electron microscopy (TEM) images of ultraminiature GNC-RGD composed of 7–8 nm GNP spheres (ci) and large GNC-RGD composed of 20 nm GNP spheres (ciii), ×2000, 20 kV; bar = 100 nm and

10 nm. (cii and civ) TEM images of GNC-RGD at higher magnification, showing the details in the red dotted square boxes in (ci) and (ciii). (d) UV-Vis absorption spectra of 7–8 nm diameter GNP monomers and ultraminiature GNC-RGD. (e) Dynamic light scattering (DLS) data showing the particles distribution of GNP monomers and GNC-RGD measured in aqueous solution. The insert images show the colloidal solutions of 7–8 nm CNP monomers (red color) and ultraminiature GNC (blue color). (f) Confocal microscope images of HUVEC, ARPE-19, and HeLa cells incubated with 100 μg/mL of non-targeting GNC (fi–fiii) and GNC-RGD (fiv–fvi) for 24 h. Yellow fluorescence reveals the location of lysosome stained by lysotracker. Blue color represents the morphology of cell's nuclei marked by DAPI. Green fluorescence shows cell's actin stained by phalloidin. Red color displays the internalized targeting ultraminiature GNC in lysosome stained by ICG dye. (g–h) PAM images of ARPE-19 cells incubated with non-targeting GNC (g) and with targeting GNC (h). Orange color specifies the internalized GNC uptake by cells. (i) Comparison of PA signals obtained from ultraminiature GNC (5nm) and large GNC (20 nm) under laser illumination at 75,000 pulses and fluence of 0.04 mJ/cm2. (j) Threshold damage of ultraminiature and large GNC. PA signals from large GNC were significantly reduced. (k) Photograph of samples before and after laser irradiation. Large GNC almost disable under 6000 pulses laser illumination of 10 mJ/cm^2 (pink color) while parts of ultraminiature GNC disassemble (blue-pink color) and confirmed by the suspension solution color shift from blue to pink. (l–o) UV-Vis absorption spectrum of large and ultraminiature GNC after laser illumination at different exposure pulses (1200, 3000, and 6000 pulses) and laser fluences (8 and 10 mJ/cm^2).

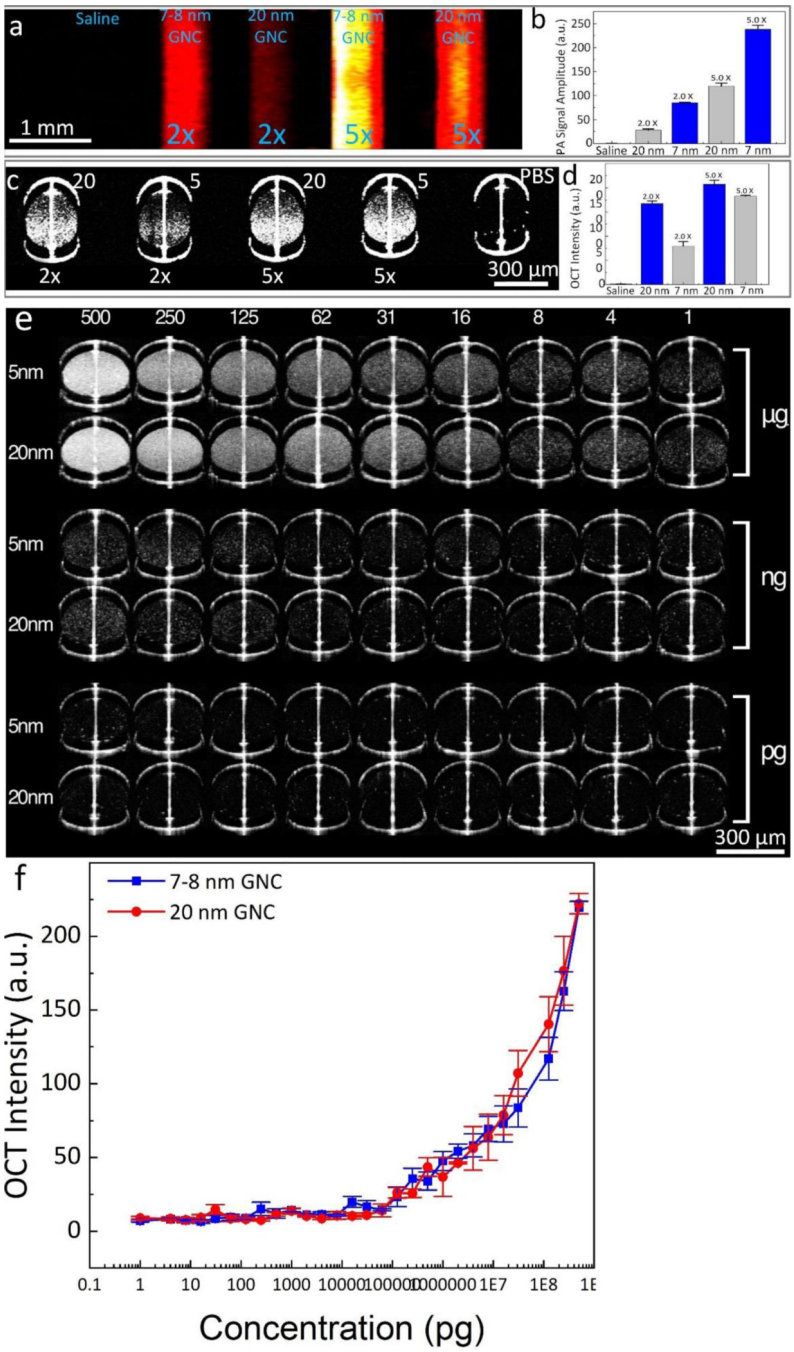

Fig. 2. Multimodal imaging system and optical properties of GNC.

(a) PAM image of phantom samples filled with saline, ultraminiature GNC, and large GNC at concentration of 2× and 5×. (b) Panel of quantitative PA signal (N=3; $p<0.01$)). (c) 2D OCT image of phantom samples. (d) Measured OCT signal intensity (N=3; $p<0.01$)). (e) 2D OCT captures of phantom samples poured with ultraminiature and large GNC at different concentrations ranging from 1–5×10^8 pg/mL. (f) quantitative OCT signal intensities were measured from 5 different locations on the OCT images. Data presents as mean±SD (N=5).

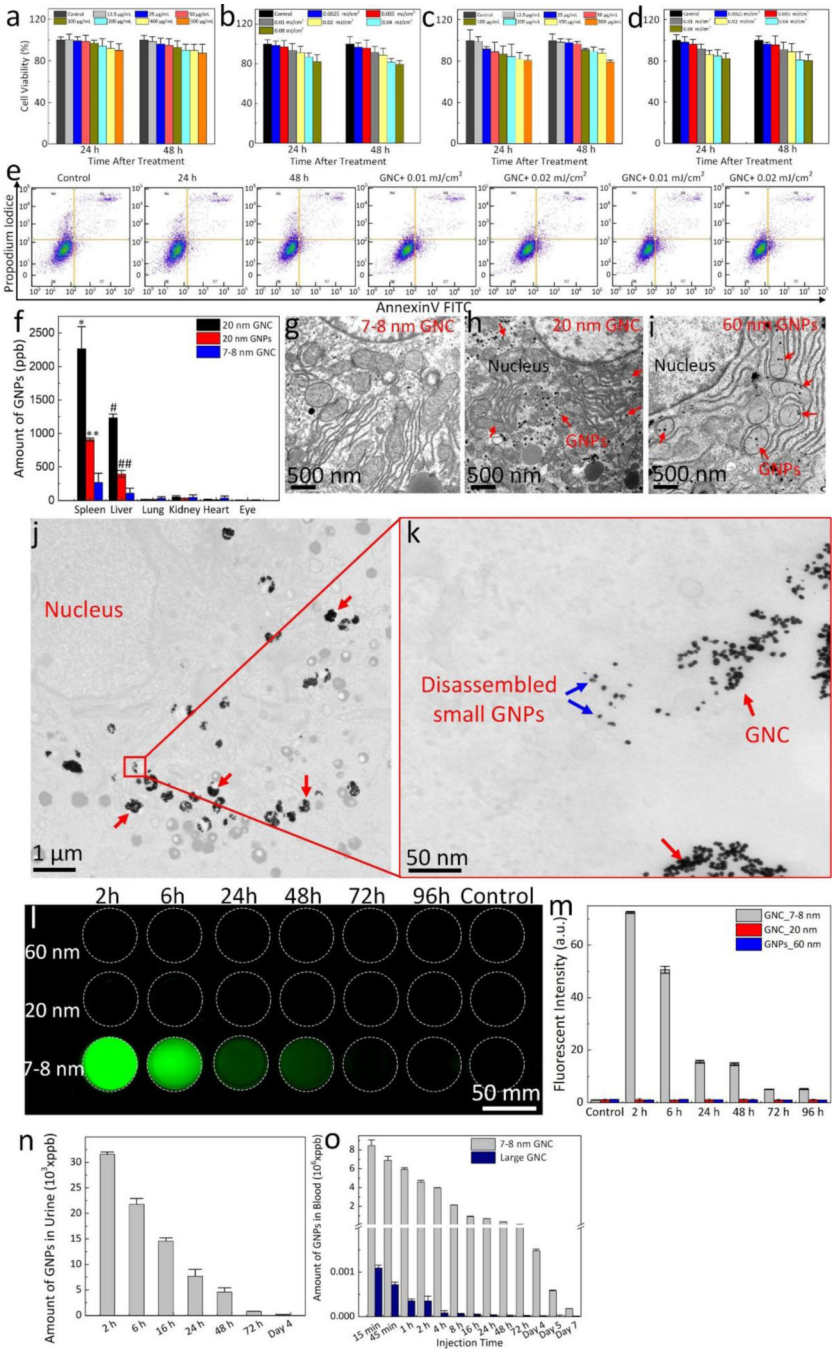

Fig. 3. Renal excretion and biocompatible assessment.

(a, c) MTT assay of ARPE-19 and HUVEC cells incubated with ultraminiature ICG-GNC-RGD at various concentrations ranging from 0 (PBS) to 500 μg/mL and treatment times of 24 h and 48 h. (b, d) MTT assay of ARPE-19 and HUVEC cells after treatment with ultraminiature ICG-GNC-RGD at 100 μg/mL followed by laser illumination at different laser fluences (i.e., 0.01–0.08 mJ/cm2). (e) Flow cytometry analysis. (f) Biodistribution of GNC in different organs. Data are shown as mean and standard deviation (SD) (N=3, *p<0.05, **p<0.01, and ***p<0.001). (g–i) Transmission electron microscopy (TEM)

images of rabbit's liver after administration of ultraminiature GNC (g), large GNC (h) and 60 nm diameter GNP monomers (i) at day 28 post injection. The large GNC and 60 nm diameter GNP monomers were found in cytoplasm (red arrows). (j) Low magnification transmission electron microscopy (TEM) image of ultraminiature GNC in ARPE-19 cells. Red arrows show the internalized ultraminiature GNC accumulated in the cytoplasm. (k) High magnification TEM image isolated from the red rectangle shown in k. Blue arrows show the distribution of disassembled nanoparticles in bioenvironment. (l) Fluorescent image of urine collected after administration of ultraminiature GNC encapsulated with RGD and ICG (ICG-GNC-RGD), large ICG-GNC-RGD, 60 nm diameter GNP monomers (60 nm), and control group (administrated with PBS) with a dosage of 400 μL at mass concentration of 5 mg/mL (400 μL) into rabbits. The green fluorescence indicates the renal excretion of ultraminiature ICG-GNC-RGD through urine.
(m) Quantitative measurement of the fluorescent intensity shown in (l). (n) Amount of GNPs in urine post administration of the ultraminiature GNC measured by wet ICP-MS method. (o) Half-life (t1/2) blood circulation of the ultraminiature GNC.

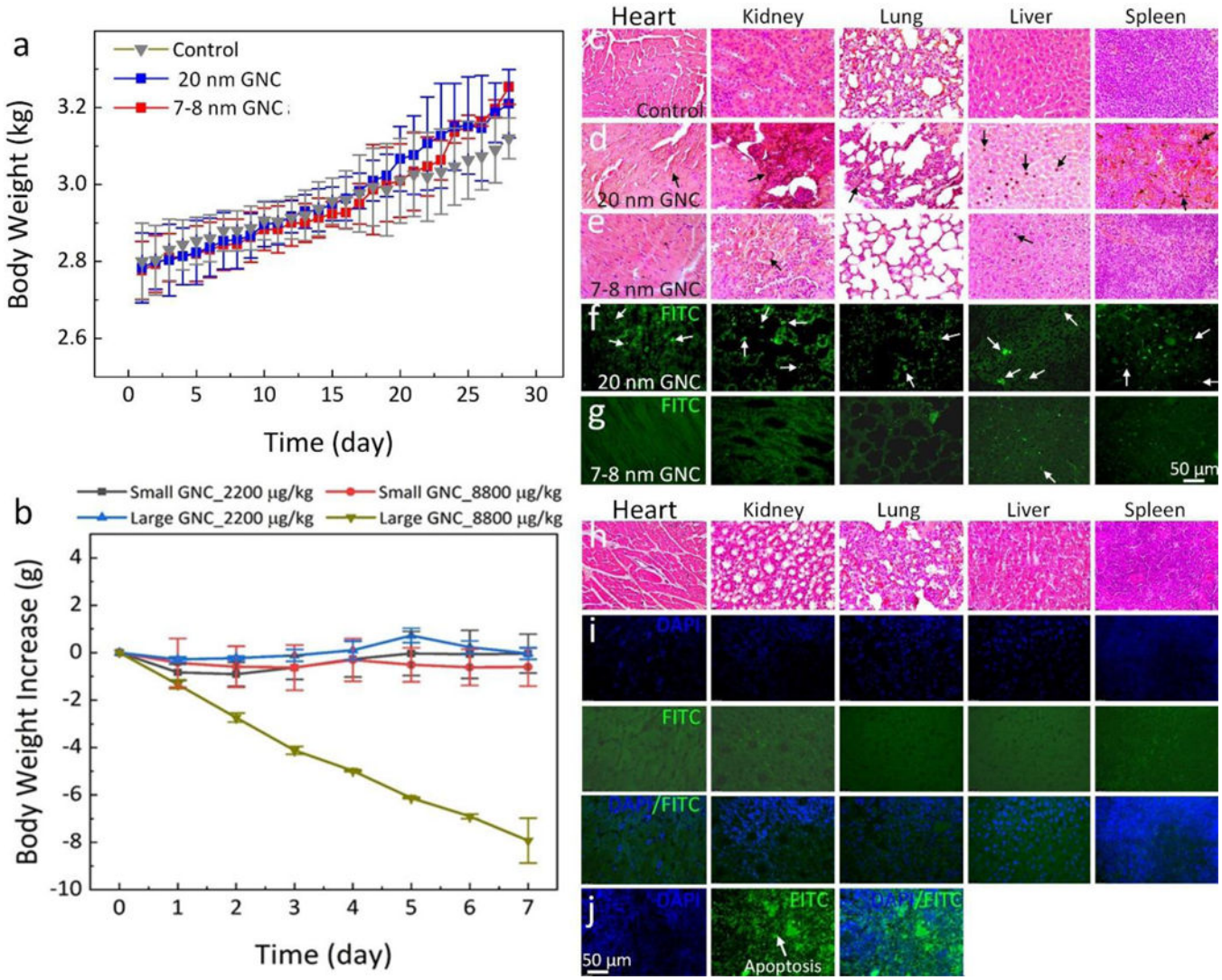

Fig. 4. *In vivo* biosafety analysis.

(a) Body weight of rabbits pre and post treatment at different time points. (b) Body weight of mice post-treatment with ultraminiature and large GNC at different concentrations (2200 and 8800 mg/kg). At the highest concentration of 8800 mg/kg, the body weight of all treated animals with large GNC rapidly decreased (N=3), but all other groups showed stable body weight. Biosafety analysis of the treated organs at highest concentration (8800 mg/kg) using H&E staining: control (c), large GNC (d), and ultraminiature GNC (e) and TUNEL assay of large GNC (f) and ultraminiature GNC (g) group. Green color indicates the apoptosis cells caused by the accumulation of GNPs. Biosafety analysis of the treated rabbit's organs using H&E staining (h) and TUNEL assay (i). (j) Positive control of spleen tissues. No evidence of the apoptosis cells was observed on the treated tissues with a low concentration of ultraminiature GNC, confirming that the ultraminiature GNC had greatly biocompatible and induced minimal toxicity to the animal. Blue fluorescence shows the cells' nuclei.

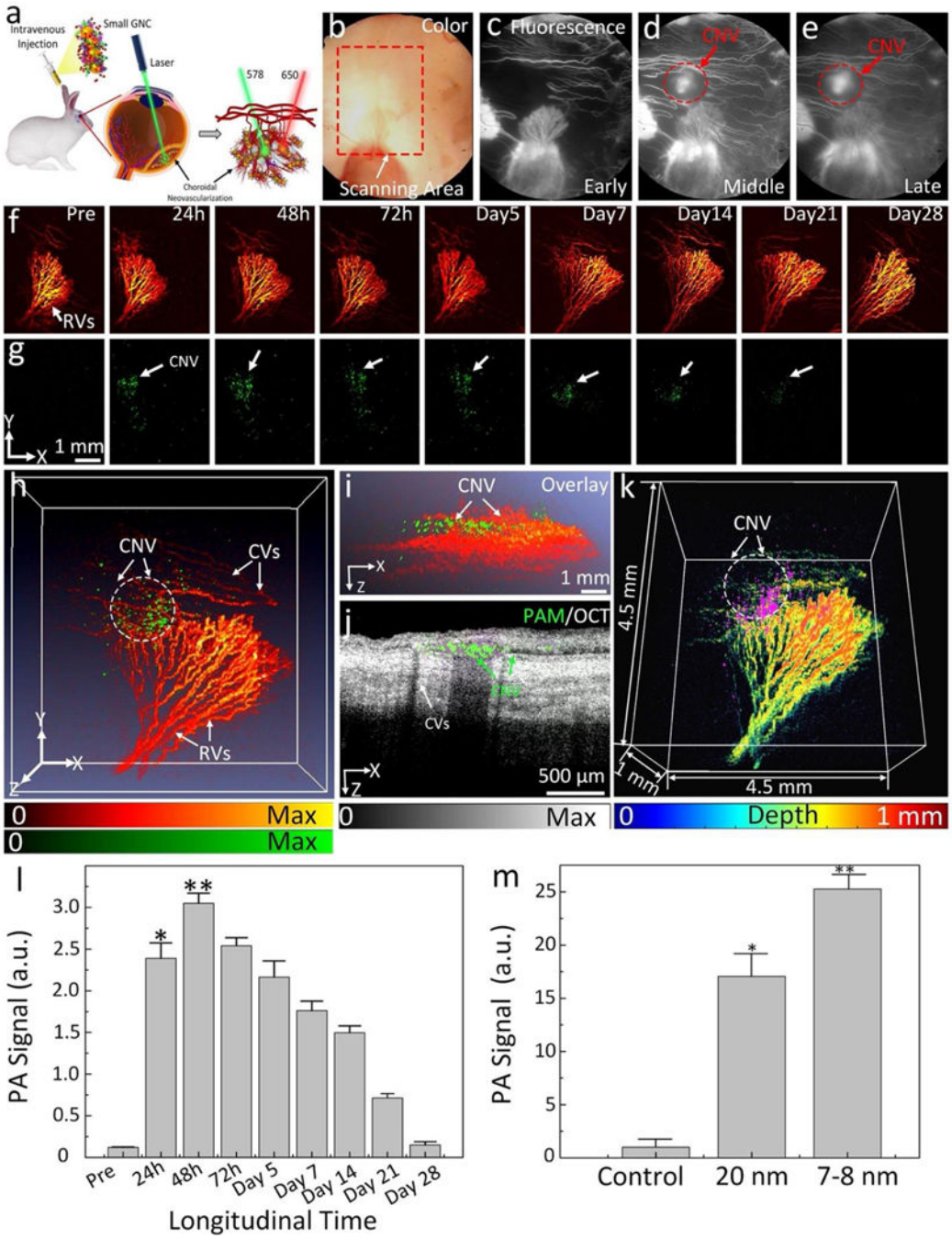

Fig. 5. In vivo CNV targeting efficiency of ultraminiature GNC in a rabbit RVO model.

(a) Illustration of GNC targeting CNV. Under nanosecond pulsed laser, GNC absorb laser energy and induce photoacoustic (PA) signals. (b) Color image obtained at day 28 post laser-induced photocoagulation or RVO model. (c–e) Fluorescein angiography (FA) images obtained at different phases: early, middle, and late. Leakage areas at middle and late phase FA demonstrate the evidence of the newly developed CNV (red dotted circles). (f–g) Maximum projection intensity (MIP) PAM images obtained along the scanning areas show in color fundus image (b) at 578 nm (f) to recognize structure of retinal vessels, choroidal

vessels, and capillaries and 650 nm (g) to observe choroidal neovascularization (CNV), respectively. Green color shows the detected CNV after administration of ultraminiature GNC. (h) Selected overlay 3D visualization of CNV obtained at 48 h. The location of CNV (white dotted circle) was clearly observed and matched well with fluorescein angiography (FA) image shown in (c)–(e). (i) XZ view of overlay PAM image. (j) Co-registered 2D OCT picture and XZ PAM picture obtained at 650 nm. (k) Depth-encoded PAM image. (l) Graph showing time-dependent PAM signal amplitude measured from the region of interests (ROIs) in (g). (m) Comparison of PAM signal amplitude achieved from three different groups: control (non-targeting ultraminiature GNC), targeting ultraminiature GNC, and targeting large GNC. Data are shown as average ± SD (N=3, $*p<0.05$).

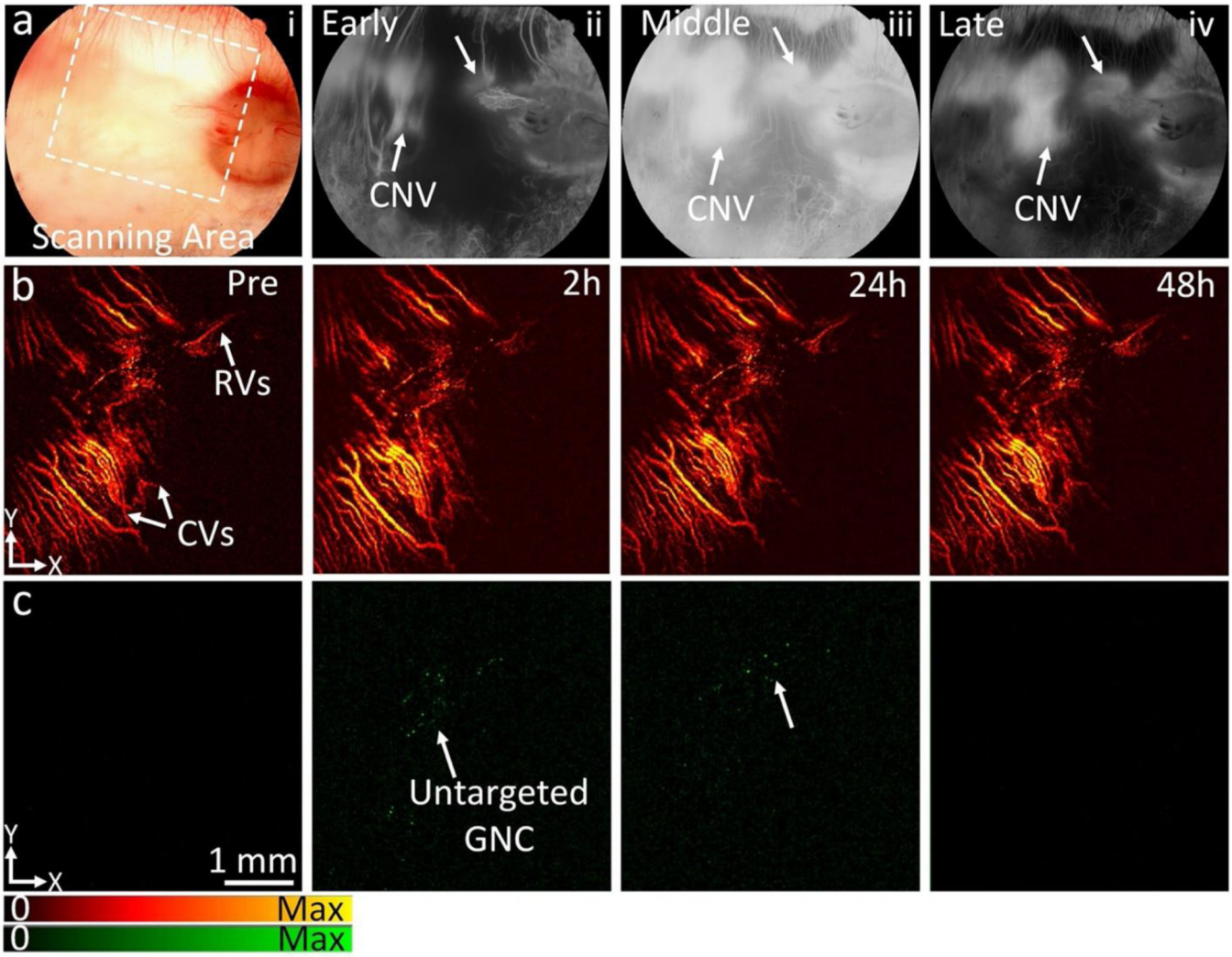

Fig. 6. *In vivo* PAM imaging of negative control group pre and post administration of non-targeting ultraminiature GNC without conjugated RGD peptides (N=3).

(a) Color fundus photography (i) of rabbit with retinal vein occlusion (RVO) model, early phase fluorescein angiography (FA) (ii), middle phase FA (iii), and late-phase FA (iv). Fundus color shows major retinal vasculature, optic nerve, and capillaries. FA images show the position of newly developed choroidal neovascularization (CNV) as depicted by white arrows. (b–c) PAM images of newly developed CNV achieved at 578 nm and 650 nm pre-and post-administration of ultraminiature GNC (0.4 mL, 5 mg/mL) at 2 h, 24 h, and 48 h. The CNV was not visualized on the PAM obtained at 650 nm after the injection of nanoparticles due to a lack of targeting peptides. The PA signal found at 2 h and 24 h post-injection may come from the extravasation of ultraminiature GNC at CNV as a result of the EPR effect.

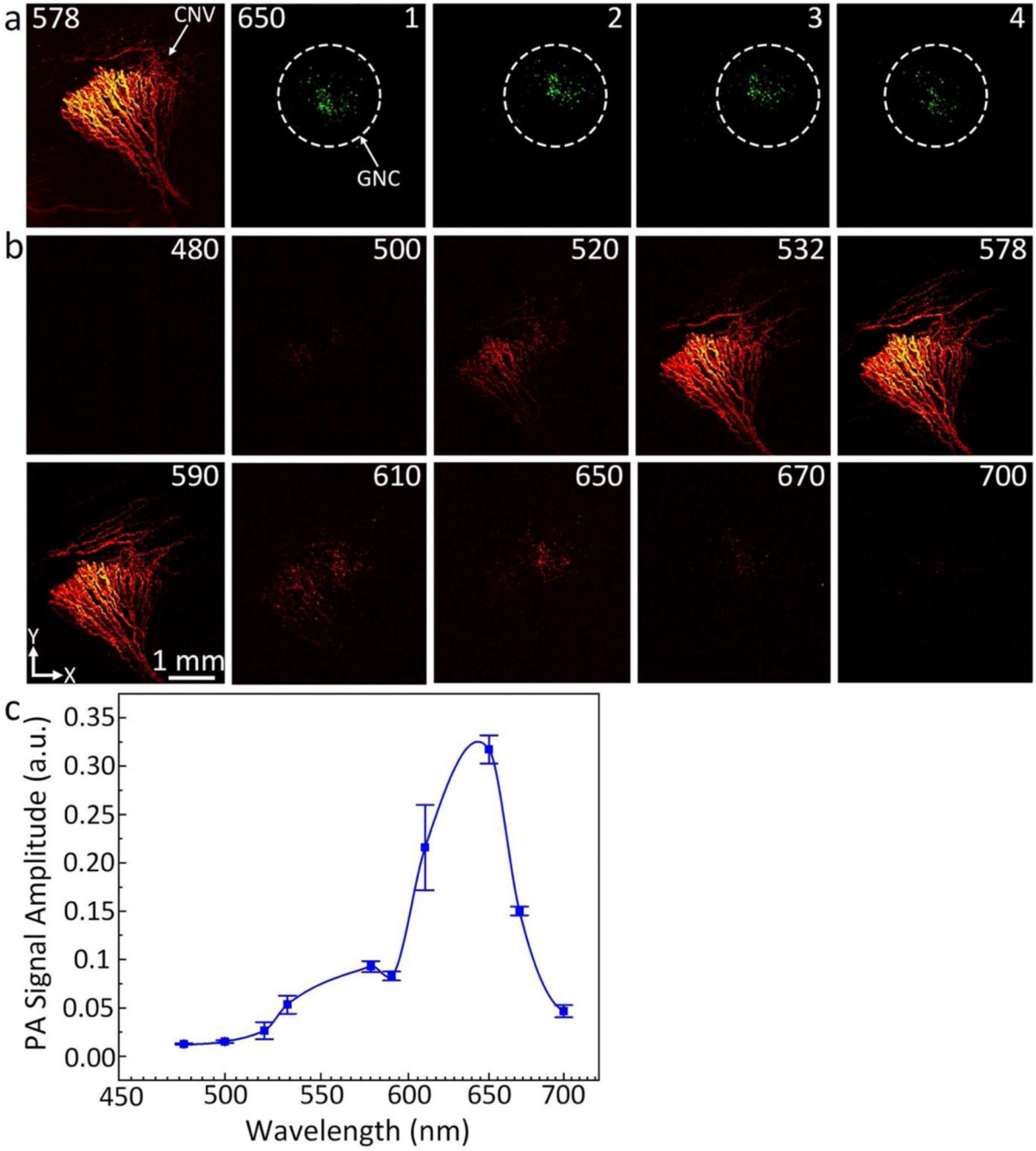

Fig. 7. ***In vivo*** **spectroscopic PAM image and photostability analysis.**

(a) PAM images were scanned along within the CNV location for different time points under the same excitation laser fluence of 0.02 mg/cm^2. PAM was first scanned at a wavelength of 650 nm 4 times and then the wavelength was turned to 578 nm to visualize the morphology of retinal, and choroidal vessels. ROI was scanned for 4 times under laser excitation with the same fluence. The acquisition time is approximately 65 s to acquire each image. (b) Spectroscopic PAM images. (c) A panel of PAM signal as a function of excitation wavelengths.

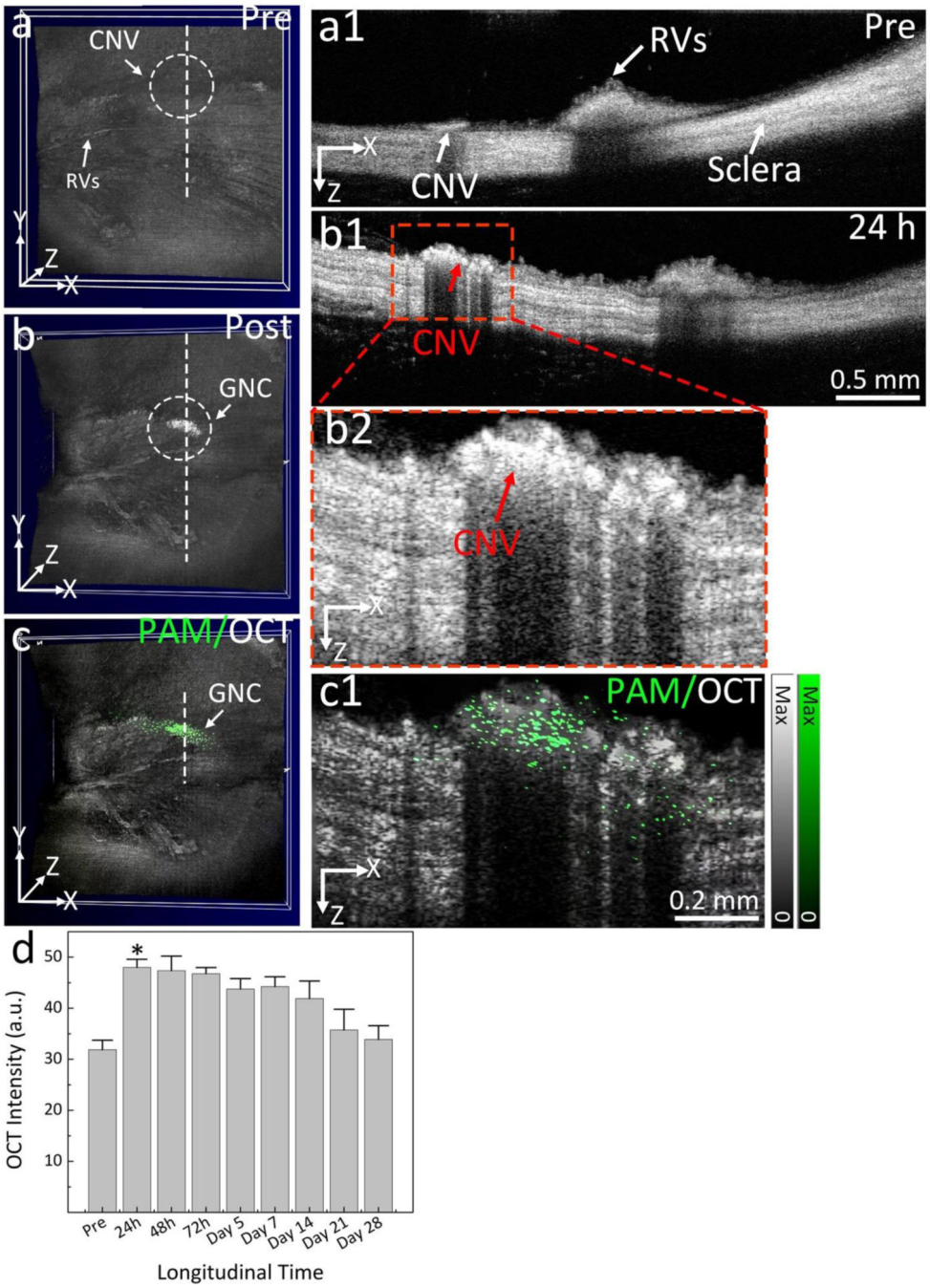

Fig. 8. ***In vivo*** **OCT images of CNV post administration of targeting ultraminiature GNC.**

(a–b) 3D volumetric OCT images acquired pre and post administration of ultraminiature GNC, respectively. White dotted circles represent the detected position of newly developed CNV. (a1) and (b1) 2D OCT images achieved along the scanning dotted line shown in (a) and (b). (b2) Magnification OCT image extracted from (b1). Red arrows exhibit the boundary and location of CNV with high hyperreflective contrast. (c) Co-registered 3D OCT and PAM image achieved at 650 nm. (c1) Cross-sectional overlay 2D OCT and PAM. Pseudo-green color demonstrates the distribution of GNC bound at CNV. (d) Graph of

OCT signal intensity measured in the region of interests (ROIs) at various time points post treatment of ultraminiature GNC. The data are shown as average ± SD (N=3, *$p<0.05$). See supplementary information for more details.

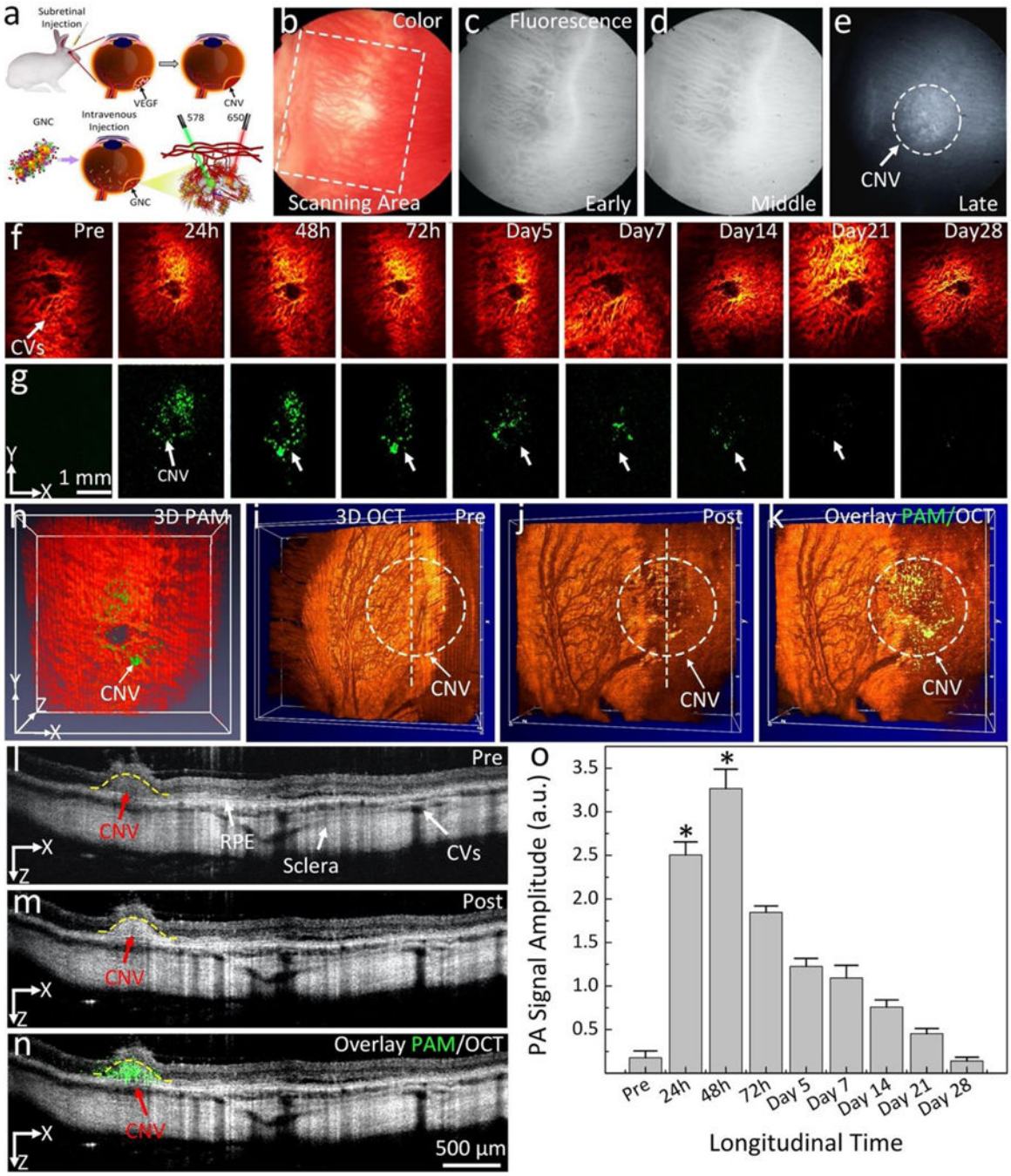

Fig. 9. *In vivo* evaluation of ultraminiature GNC cluster targeted CNV in rabbit with subretinal injection of VEGF model.

(a) Schematic of subretinal injection of VEGF into subretinal space followed by IV administration of targeting GNC. (b–e) Color fundus image of the retina (b) and indocyanine green angiography (IGCA) images obtained at early (c), middle (d), and late phase (e) before administration of ultraminiature GNC. The early and middle phase fluorescent images clearly show morphology of choroidal vessels. The late phase ICGA shows the detected CNV (white dotted circle). (f–g) PAM images achieved at 578 nm and 650 nm, respectively. The location of CNV after treatment was marked as white arrows. (h) Selected

overlay of 3D PAM images at 578 nm and 650 nm. (i–j) 3D volumetric OCT images achieved pre and post treatment, respectively. White dotted circle shows the position of CNV. (k) Merged PAM and OCT image. (l–m) 2D OCT images before and after treatment showing different retinal layers such as RPE, choroid, choroidal vessels, CNV and sclera. (n) Co-registered 2D PAM and OCT images. Green color indicates the accumulation of ultraminiature GNC at the CNV lesion. (o) Quantitative measurement of the PAM signals in CNV obtained at various time points: Pre, 24, 48, 72 h and days 5, 7, 14, 21, and 28. The data are shown as average ± SD (N=3). * is for $p<0.05$. See supplementary information for more details.